Aalborg Universitet

AALBORG UNIVERSITY
DENMARK

Correction of motion effects in free breathing thoracic CT and PET imaging for radiotherapy

Nielsen, Martin Skovmos

CORRECTION OF MOTION EFFECTS IN FREE BREATHING THORACIC CT AND PET IMAGING FOR RADIOTHERAPY

ASSESSMENT OF UNCERTAINTIES USING FDGPET, FIDUCIALS AND ANATOMICAL LANDMARKS IN RADIOTHERAPY PLANNING

BY
MARTIN SKOVMOS NIELSEN

AALBORG UNIVERSITY
DENMARK

CORRECTION OF MOTION EFFECTS IN FREE BREATHING THORACIC CT AND PET IMAGING FOR RADIOTHERAPY

- ## ASSESSMENT OF UNCERTAINTIES USING FDG-PET, FIDUCIALS AND ANATOMICAL LANDMARKS IN RADIOTHERAPY PLANNING

by

Martin Skovmos Nielsen

AALBORG UNIVERSITY

DENMARK

Dissertation submitted 20 July, 2016

.

CV

Name	Martin Skovmos Nielsen
Address	Bæveren 40 9530 Støvring Denmark
Education	2007 Medical Physicist, Oncology 2002 MSc Physics, Aalborg University, Denmark
Present employment	Dept. of Medical Physics, Aalborg University Hospital

Published papers

1. **Nielsen MS**, Ostergaard LR, Carl J. A new method to validate thoracic CT-CT deformable image registration using auto-segmented 3D anatomical landmarks. Acta Oncol 2015;54(9):1515-20.

2. **Nielsen MS**, Nystrom MW, Carl J. Potential position errors using fiducial markers for gated image guided radiotherapy. Acta Oncol 2013 Oct;52(7):1472-6.

3. Carl J, Nielsen J, **Nielsen MS**, Zepernick PR, Kjaergaard B, Jensen HK. A new lung stent tested as fiducial marker in a porcine model. Rad. Oncol 2012 Feb;102(2):297-302.

4. Kjaergaard B, Zepernick PR, **Nielsen MS**, Jensen HK, Arp DT, Thomsen JB, et al. Apneic Oxygenation in Diagnosis and Treatment of Lung Tumours in an Experimental Porcine Model. Scan J. of Lab. Animal Science 2012 Jan 1;39(1):103-10.

5. Poulsen PR, Carl J, Nielsen J, **Nielsen MS**, Thomsen JB, Jensen HK, et al. Megavoltage image-based dynamic multileaf collimator tracking of a NiTi stent in porcine lungs on a linear accelerator. Int J Radiat Oncol Biol Phys 2012 Feb 1;82(2):e321-e327.

6. Carl J, Jensen HK, Nielsen J, **Nielsen MS**, Schmid M, Siegfried L. A New Fiducial Marker for Gated Radiotherapy in the Lung – A Feasibility Study of Bronchoscopy Based Insertion and Removal in Göttingen Mini-Pig. Scan. J of Lab. Animal Science 2010;37(2):117-27.

7. **Nielsen MS**, Carl J, Nielsen J. A phantom study of dose compensation behind hip prosthesis using portal dosimetry and dynamic MLC. Rad. Oncol. 2008 Aug;88(2):277-84.

ENGLISH SUMMARY

Of the thoracic cancers, lung cancer has the highest incidence in both genders. For accurate diagnosis and staging, positron emission tomography (PET) and computed tomography (CT) are currently the most suitable imaging modalities for the thorax. For lung cancer diagnosis with lymph node extension added to the clinical target volume (CTV), the optimal treatment regime, is combined chemotherapy and external radiotherapy. For external radiotherapy, the respiratory motion of the thorax can result in image artefacts and thereby introduce potential misinterpretation of the target lesions and organs at risk. A common method to reduce motion-induced image artefacts is respiratory-correlated 4D image acquisition. In radiotherapy, the use of 4D-PET/CT potentially reduce the CTV safety margin when combined with respiratory-correlated image guided radiotherapy (IGRT). Margin reduction is crucial, as reported toxicity following radiotherapy is a dose-limiting factor. To minimize the safety margins in radiotherapy, accurate target and normal tissue identifications is essential for any image modality. Still, the margin must be sufficient to cover the uncertainties related to target definition and the daily target detection during a course of radiotherapy.

The main purposes of this project were assessments of uncertainties in respiratory-gated image guided radiotherapy using PET imaging for target definition, fiducials as target surrogates and deformable CT-CT image registrations.

Paper I describes the evaluation of the uncertainties using fiducials for planning and delivery of gated IGRT. The uncertainties related to 4D-CT detection of fiducials was correlated to fiducial speed within phase bin acquisition, fiducial orientation and fiducial type/size. Increased uncertainties were observed for the following: fiducials detected within CT phase bins acquired outside the inhalation and exhalation CT phases, small and less dense fiducials, and fiducials oriented at 45° relative to the motion trajectory. Minor detection uncertainties of the fiducials were related to respiratory-gated image guidance using stereoscopic X-ray verification images. Paper II describes the assessed dissimilarities between commonly used PET segmentation methods for target lesions affected by respiratory motion in combination with heterogeneous tracer uptake values. Respiratory correlated 4D-PET images provided for each segmentation method results nearly equivalent to static PET images. When motion correction was available for 3D-PET images the most consistent and lowest segmentation variation was accomplished with the GradientSeg method. For motion disturbed 3D-PET images, severe misinterpretations were observed with the GradientSeg method, and therefore the 2.5SUV method was preferred. A validation method using extracted anatomical landmarks for thoracic CT-CT co-registrations was described in paper III. Three

subsequent thoracic CT scans were co-registered using the B-spline, Demons and Affine image registration methods. The accuracy of these registrations was assessed by volume similarities and deviations between corresponding landmarks. Anatomical features extracted from the bronchial tree provided a 3D grid of bronchial branch points as landmarks. The overall deviation between corresponding landmarks was lower for registration methods using local deformations. In contrast, the maximum discrepancies between corresponding landmarks were also detected for the registration methods using local deformations. The bronchial branch points provided anatomical features that were useful as a validation method and for identification of local registration errors missed by volume similarity assessments.

DANSK RESUME

Blandt kræft i thorax regionen har lungekræft den højeste incident for begge køn. For at kunne stille en præcis diagnose for kræft i thorax regionen er de mest oplagte billede teknikker positron emission tomography (PET) og computed tomography (CT). Den optimale behandling af lungekræft, hvor kræften har spredt sig til de nærliggende lymfeknuder, er en kombineret behandling bestående af kemoterapi og strålebehandling. Vejrtrækningsbevægelser i thorax regionen kan resultere i billedeforstyrrelser og eventuelt fejlfortolkning af kræftvæv og risiko-organer. Ofte anvendes vejrtrækningskorreleret 4D billede-teknikker til at minimerer billedeforstyrrelser. Anvendelse af 4D-PET/CT kan reducere den nødvendige sikkerhedsmargin der anvendes ved stråleterapi – især kombineret med vejrtrækningskorreleret billedevejledt strålebehandling (IGRT). Begrænsning af sikkerhedsmargin er særligt betydningsfuldt ved stråleterapi idet bivirkningerne er dosisbegrænsende. Til at mindske bivirkninger efter stråleterapi er det for alle billedteknikker nødvendigt med nøjagtig identificering af både kræftvæv og risiko-organer. Men indenfor stråleterapi skal sikkerhedsmarginen stadig dække de usikkerheder der er forbundet til detektion af kræftvæv og fusioneringer af de daglige billedevejledte korrektioner gennem strålebehandlingsforløbet.

Hovedformålet for denne afhandling er en beskrivelse af usikkerheder forbundet til vejrtrækningskorreleret billedevejledt strålebehandling med PET billeder til definition af kræftvæv, markører som surrogat for kræftvæv og fusionering mellem CT-CT billeder.

Artikel I beskriver evaluering af usikkerheder ved brug af markører til planlægning af strålebehandling og behandling med vejrtrækningskorreleret IGRT. Detektionsusikkerheder for markører i 4D-CT var associeret til markør fart under billeoptagelse, markør orientering og markør type/størrelse. De observerede usikkerheder øges ved: Markører detekteret i CT faser der ligger udenfor maksimal ind- og udånding, små markører med lille massefylde samt markører der ligger orienteret i en vinkel på 45 grader i forhold til bevægelsesretningen. Mindre detektionsusikkerheder for markørerne blev relateret til vejrtrækningskorreleret billedevejledning. I artikel II vurderes forskellen mellem ofte anvendte metoder til segmentering af kræftvæv i PET billeder under indflydelse af både respirationsbevægelse og uensartet optag af sporstof. Ved brug af vejrtrækningskorreleret 4D-PET viser segmenteringerne at være stort set identiske med statiske 3D-PET billeder for alle metoderne. Kun GradientSeg metoden viser resultater svarende til statiske 3D-PET billeder ved bevægelses-korrigeret 3D-PET billeder. GradientSeg metoden viser dog store afvigelser i 3D-PET billeder der indeholder bevægelser, sammenholdt med statiske 3D-PET billeder. Det anbefales for denne type PET billeder at anvende 2.5SUV metoden. I artikel III beskrives en

valierings metode for anatomiske markører, der anvendes til kontrol af CT-CT billede fusionering. Fem patienter, hver bestående af tre efterfølgende CT billeder af thorax, fusioneres hver især med metoderne B-spline, Demons og Affine. Nøjagtigheden af disse billede-fusioneringer vurderes på baggrund af volumen sammenligninger samt afgivelser mellem tilsvarende anatomiske markører. De anatomiske markører blev defineret i form af et 3D gitter bestående af forgreningspunkter i lungetræet. Overordnet var afstande mellem tilsvarende forgreningspunkter mindst for fusioneringsmetoder der tillader lokale deformationer. Dog fremkom de største afvigelser mellem tilhørende forgreningspunkter for netop fusioneringsmetoder med lokale deformationer. Lungetræets forgreningspunkter giver mulighed for at kontrollere billedefusioneringer på baggrund af anatomiske markører, herunder identifikation af lokale fusioneringsfejl der ikke ses ved volumen sammenligninger.

ACKNOWLEDGEMENTS

ABBREVIATIONS

3D-CT	Three-dimensional Computed Tomography
4D-CT	Four–dimensional Computed Tomography
3D-PET	Three-dimensional Positron Emission Tomography
4D-PET	Four-dimensional Positron Emission Tomography
CTV	Clinical Tumour Volume
DICOM	Digital Imaging and Communication in Medicine
DIR	Deformable Image Registration
DVH	Dose Volume Histogram
EUD	Equivalent Uniform Dose
GM	Gold Marker seed
GTV	Gross Tumour Volume
HU	Hounsfield Unit
IGRT	Image-Guided Radiotherapy
IMRT	Intensity-Modulated-Radiotherapy
FDG	F-18 Fluorodeoxyglucose
KV	Kilo Voltage
MRI	Magnetic Resonance Imaging
MV	Mega Voltage
NiTi	Nickel Titanium
NTCP	Normal Tissue Complication Probability

OBI   On Board Imaging

OAR   Organ At Risk

PTV   Planning Target Volume

SBRT   Stereotactic body radiotherapy

RPM   Real-time Position Management

TCP   Tumour Control Probability

VOI   Volume Of Interest

TABLE OF CONTENTS

CORRECTION OF MOTION EFFECTS IN FREE BREATHING THORACIC CT AND PET IMAGING FOR RADIOTHERAPY

CHAPTER 1. INTRODUCTION

Lung cancer is the most prevalent malignant cancer type located in the thoracic region. The majority part of diagnosed lung cancer patients are elderly patients, likely suffering of multiple co-morbidities as chronic obstructive pulmonary disease or heart disease. Dispite new treatment modalities for lung cancer patients with improved local control rate, the overall survival rate are low with 5-years survival rate of 10-15 % (1). In general, curative cancer treatment is a balance between increasing tumour control while preventing toxicity in the surrounding tissue, called the therapeutic window. For patients with limited diseases, young age or appropriate performance status, the treatment strategy may be aggressive with respect to the different treatment modalities and treatment doses (radiotherapy and chemotherapy). However, normal tissue complications and co-morbidities may be limiting factors for the choice of treatment. Preventing undesirable toxicity is a primary goal for every treatment modality. For thoracic cancer patients, pulmonary injuries are the primary concern, as the lung is both a target and an organ at risk (OAR). A high risk of lung damage may lead to a less aggressive treatment regimen and a potentially lower rate of cancer cure. On the other hand, the target margins for radiotherapy must still be large enough to cover the target and cure the patient.

The foundations for radiotherapy planning rely on correct OAR and target volume identification. Consequently, accurate and high-quality image modalities are essential for the planning phase. Precise image acquisition provides images analogous to a patient's anatomy during each treatment session. High-quality images are essential for precise and consistent target detection as well as to differentiate healthy and malign tissue. In radiotherapy, target of thoracic situated cancers are usually identified using computed tomography (CT) combined with F-18 fluorodeoxyglucose (FDG) positron emission tomography (PET). Due to respiratory motion, images of lung cancer patients may suffer from motion blur or geometrical misalignment of the target site during image acquisitions. The fast CT and the slow PET acquisitions can in different ways lead to variation and inconsistency of OAR- and target volume determination. These variations provide uncertainties, which needs to be described for optimal radiotherapy.

The purpose of this PhD research project was to assess uncertainties related to radiotherapy preparation for patients with cancer located in the thoracic region. To assess these uncertainties, the primary focus was on CT-based image detection of fiducials, anatomical landmarks for image registration, and FDG-PET image segmentations of lesions with inhomogeneous tracer activity.

CORRECTION OF MOTION EFFECTS IN FREE BREATHING THORACIC CT AND PET IMAGING FOR RADIOTHERAPY

CHAPTER 2. LUNG CANCER

In Denmark 4485 (12% of all cancers) newly diagnosed lung cancers have been registered per year, with an almost equal distribution between the genders (2). For men, lung cancer has the highest incident rate of all cancers worldwide (34 per 100 000) (1). Though lung cancers are the most prevalent of the thoracic cancers, several thoracic cancers are related to pleural mesothelioma and lymphomas. In Denmark, 113 (0.3% of all cancers) newly diagnosed pleural mesothelioma and 1083 (3% of all cancers) Non-Hodgkin Lymphoma cases were identified in 2010 (1). Lung cancer is divided into two main groups defined as small cell lung cancer (SCLC) and non-small cell lung cancer (NSCLC). Roughly, 10-15% of lung cancers are diagnosed as SCLC; consequently, a majority of lung cancer is classified as NSCLC. The incidence rates have been falling for men since the 1990s, whereas for women, the incident rate still climbs. At present, the annual death rate of lunge cancer is approximately 50 per 100 000 for both genders, whereas the death rate for males in the 1990s were above 80 per 100 000 (1;3).

2.1. ETIOLOGY

Most pulmonary cancers are associated to smoking, with reported lung cancer responsibility in the range of 70-90% (4;5). However, other risk factors such as age, asbestos, radon gas, pollution and chemical exposure, have been associated as risk factors for lung cancers (3). Whereas smoking is classified as a life style risk factor, exposure to asbestos and chemical compounds are likely to be work related risk factors, whereas radon gas and pollution probably relate to residence location.

2.2. DIAGNOSIS

For patients suspected of having lung cancer, an X-ray examination is recommended. If the X-ray image indicates a lung infiltrate or shadow, further investigation is required. The sequence for a lung cancer examination is a CT scan, a pulmonary function test and a bronchoscopy examination including tissue biopsy. A full body FDG-PET scan support the diagnostic CT for potential metabolic metastases detection. The biopsy includes mediastinal lymph node examination for potential dissemination verification.

2.3. CLASSIFICATION

The clinical staging of lung cancer follows the TNM classification system in which
T-stage describes the extent of the primary tumour, the N-stage the extent of nodule
involvement and the M-stage the extent of distant metastases (6). In Denmark, if
surgery is excluded, patients with NSCLC stage T1-2aN0M0 are offered
stereotactic body radiotherapy, and conventional radiotherapy is suggested for stage
T2B-3B or nodular extension (7).

2.4. TREATMENT OF LUNG CANCER

Treatment of lung cancer differs between the two main groups. SCLC consists of
rapidly proliferating homogeneous cells that have a higher response to
chemotherapy. However, compared to the NSCLC, the overall treatment response
for SCLC is low, except for limited disease. Chemotherapy is suggested for both
the SCLC and the NSCLC. For NSCLC, the 2-years survival increases by
aproximately 10% for patients treated with combined chemo-radiotherapy relative
to radiotherapy alone (8;9). If possible, surgery is offered as lobectomy, where the
involved lope is removed or segmentectomy removing the cancer site with a
margin. Different approaches are available for lobectomy as either open surgery,
video assisted surgery or robot surgery (10;11). Surgery, as lobectomy is limited to
early staged cancers with no lymph node involvement or metastases. For patients
with lung cancer suitable for surgery (up to T4 staging), the 5-year survival
prognosis is approximately 30% for SCLC and 50% for NSCLC (2). Depending of
the lung cancer classification, the primary choice of treatment is surgery followed
by stereotactic body radiotherapy (SBRT) (12). High-dose conventional
radiotherapy of 80 Gy (35-40 sessions) versus SBRT of 45-66 Gy (3 sessions),
revealed for limited disease T1-2 NSCLC superior SBRT survival prognosis (13).
Frequent toxicities following SBRT, are reported as rib fracture, dyspnea,
ventricular trachycarida (14) and for increased target volume pneumonitis (15;16).
A recent alternative treatment method to SBRT is radiofrequency ablation (17-19).
Radiofrequency ablation is a percutaneous CT guided technique to position the
probe for ablation into the cancer tissue. This method have shown promising result
for small target volume and might be considered as an option for inoperable lung
cancer patients. The standard treatment for patients with localized inoperable lung
cancers, i.e., lymph node involvement, is combined chemotherapy and
radiotherapy. Radiotherapy doses in Denmark are typically 45 Gy (30 sessions) for
SCLC and 66 Gy (33 sessions) for NSCLC (7).

CHAPTER 3. RADIOTHERAPY

External radiotherapy of the thorax is often planned as 3D conformal radiotherapy or intensity modulated radiotherapy (IMRT) using a number of stationary beam angels or by Volumetric Modulated Arc Therapy (VMAT). An optimal dose plan for radiotherapy is designed to ensure the prescribed dose reaches the target volume while sparring healthy tissue. Uncertainties within the target definition, patient and organ motion as well as Image Guide Radiotherapy (IGRT) all contribute to determining the target margin. Consequently, the amount of healthy tissue exposed during radiotherapy may limit the target dose or lead to undesired toxicity. Reducing the treatment margins is therefore essential, particularly because the combination of lung volume and accumulated dose correlate to the risk of radiation-induced pneumonitis (15;20;21).

Similar to diagnostic image acquisition, supplementary image modalities such as FDG-PET support CT-based radiotherapy planning (22;23). The diagnostic PET/CT might be registered to the planning CT, or a new combined PET/CT could be acquired for radiotherapy purposes alone. The combined PET/CT scanner provides unchanged patient immobilization during the whole scan procedure. Consequently, co-registration between the PET and CT images can be implemented using hardware registration due the common reference setting. In contrast, multiple image acquired beyond time intervals suitable for patient immobilization require additional software for proper image alignment. In the thorax, respiratory motions may add further uncertainties to multiple image acquisitions. As respiratory motion is present in both image acquisition for treatment preparation and image guidance during radiotherapy, disregarding respiratory motion can lead to undesired safety margins and insufficient dose coverage of the clinical target voume (CTV). A method to manage respiratory motion in diagnostic radiotherapy and radiotherapy planning is respiratory correlated four-dimensional (4D) scan acquisition (22;24;25). Modern techniques to focus radiotherapy on accurate target localization during the course of multiple treatment sessions are available as kilo-voltage (KV) or mega-voltage (MV) IGRT.

3.1. MARGINS IN RADIOTHERAPY

The target volume for thoracic cancers follows ICRU report 62 defining gross tumour volume (GTV) towards planning target volume (PTV) (26). The GTV covers the primary tumour and the involved lymph nodes. An additional margin from the GTV, including subclinical malignant tissue, defines the CTV. The CTV

include microscopic tumours cells that have spread from the GTV. Finally, the PTV includes alignment uncertainties, motion, and technical deviations.

Uncertainties in radiotherapy can be described by adding systematic and random errors in terms of standard deviations. Systematic errors are defined as standard deviation of the means between the reference conditions (planning CT) and the actual treatment conditions (radiotherapy sessions). For instance, target definition, patient immobilisation and respiratory motion may create deviations between the planning condition and the radiotherapy sessions. To reduce systematic errors, imaging under the reference conditions must agree with the radiotherapy conditions. This could for instance involve time resolved imaging for moving targets and functional image protocol to ensure detection of potential malignant cells. The source of random errors could be equal to the source of systematic errors. The difference is that random errors are related to the session-to-session variation during the course of radiotherapy. A way to reduce the session-to-session variantion could be by monitoring and correcting the patient setup and target position in each treatment session.
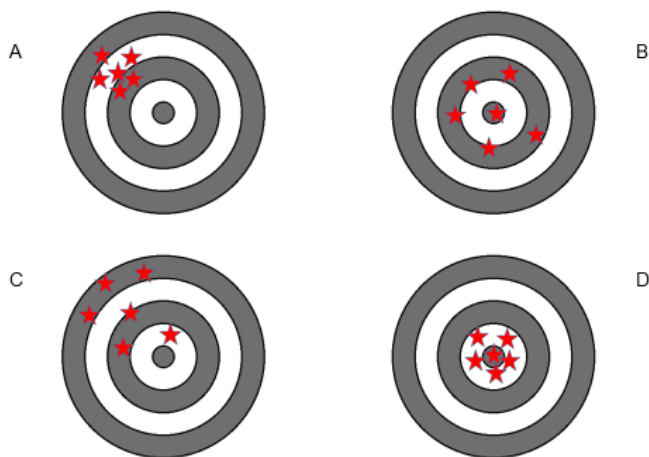
Figure 1. Distribution of systematic and random errors denoted as stars close to bull's eye. A: Large systematic and low random errors. B: Low systematic and large random errors. C: Large systematic and large random errors. D: Low systematic and low random errors.

Given the uncertainties, it may be possible to add margin to the target to account for these uncertainties. In principle, the margins in radiotherapy certify a confident planned dose for a given population of patients scheduled for radiotherapy. One way of calculating the margin (M) was proposed by van Herk et al. (27) who

suggested adding the sum of systematic (Σ) and random (σ) standard deviations linearly as

$$M = a_1\Sigma + a_2(\sigma - \sigma_p) \qquad \text{Eq. 3.1}$$

where the sum of standard deviations Σ and σ are defined as a squared sum of all systematic and random errors as

$$\Sigma^2 = \Sigma_d^2 + \Sigma_s^2 + \Sigma_m^2 \qquad \text{Eq. 3.2}$$

$$\sigma^2 = \sigma_s^2 + \sigma_m^2 + \sigma_p^2 \qquad \text{Eq. 3.3}$$

The indicies d, s, m and p are related to delineation, setup, motion and penumbra errors. The parameter a_1 for systematic errors depends on the fraction of patients intended for the described minimum dose. The parameter a_2 depends on the preferred minimum dose coverage of the CTV. The value of a_1 obtained by van Herk et al. ranged from 1.28Σ (1D and 80% of the patients) to 3.36Σ (3D and 99% of the patients). For the random uncertainties, the parameter a_2 ranged from $0.84(\sigma-\sigma_p)$ at 80% dose level to $2.34(\sigma-\sigma_p)$ for 99% dose coverage. To minimize the margin and thereby normal tissue doses, the pragmatic considerations balanced the weight of the a_1 and a_2 parameters. For the instance, a 3D conformal radiotherapy with dose homogeneity from 95-107% of the prescribed dose (28), provided to 90% of the patient population corresponded to $a_1 = 2.5$ and $a_2 = 1.64$. With the main weight given to the systematic errors, reducing the systematic uncertainties was the most effective way to limit normal tissue doses.

3.2. NORMAL TISSUE

Normal tissue is defined as any tissue outside the defined target volume intended for radiotherapy. For thoracic cancer patients, normal tissue would be tissue such as the spinal cord, lungs, oesophagus, heart and blood vessels as well as residual connective tissue. After thoracic radiotherapy, normal tissue complication such as pulmonary pneumonitis, heart- and oesophagus injuries are the most commonly reported toxicities (20;29-31). For precise assessment of radiotherapy doses to normal tissues, an accurate system of image registration and dose reporting is essential (32). Correct image registration is fundamental for both dose accumulation and tissue identification between multimodal image acquisitions. To predict normal tissue complications, a model to correlate dose accumulation and volume dependency is necessary. The Lyman-Kutcher-Burman (LBK) model is a widely used method to describe normal tissue complication probability (NTCP) in radiotherapy (33;34). The LBK model uses a translation of the dose-volume-

histogram (DVH) into a single dose for the whole organ, such as for instance a mean or equivalent-uniform-dose (EUD).
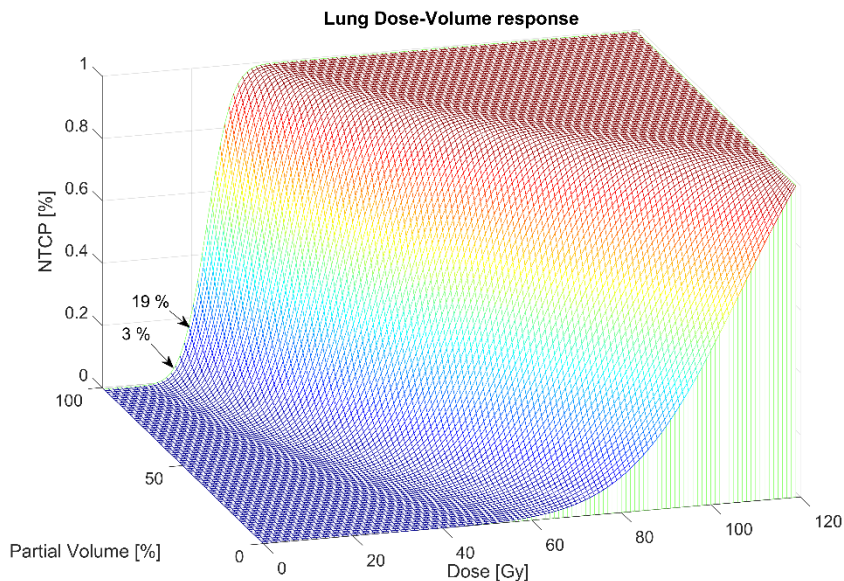
Figure 2: NTCP relation to the combined dose-volume of the lungs. Treatment planning systems can provide 2D-DVH for the organ of interest, which can be reduced to a single uniform dose given to the whole organ (100% partial volume). The two arrows specify EUD of 15 Gy respective 19 Gy and the corresponding NTCP values.

To simplify the combined dose-volume dependency, a DVH reduced into a single uniform dose given to the whole organ (partial volume = 100%) can be used (35;36). To add a 5mm isotropic margin to a target of 102cc in a lung volume of 3300cc, the lung EUD may change from 15Gy to 19Gy. Using the data from Emami et al., this EUD change corresponds to a theoretic increase of the NTCP from 3% to 19% (36). Consequently, uncertainties leading to the OAR receiving increased doses must be described according to the procedures used for performing radiotherapy and updated whenever modifications are needed. NTCP modelling of the correlation between dose and volume to the risk of pneumonitis does not provide unique parameter identification. The volume of a given dose is expressed as V_{Dose} and the mean lung dose (MLD) both associated to the risk of pneumonitis (20;37-39).

3.3. IMAGE ACQUISITION FOR RADIOTHERAPY PLANNING

Patients intended for radiotherapy are frequently immobilised with the arms above the head in a supine position. Matching patient support systems are used at the treatment facilities, as equivalent patient position is crucial. For radiotherapy, a Hounsfield unit (HU) calibrated planning CT is acquired, for both target delineation and dose calculation. Due to the low soft tissue contrast in CT images, a supplementary FDG-PET scan may support the CT for target delineation. These associated PET and CT scans can be acquired in sequence within the same frame of reference, using an integrated PET/CT scanner or by co-registering a separate diagnostic PET/CT to the planning CT. These combined PET-CT images have been shown to reduce the inter-observer variation and provide higher accuracy for TNM-staging (40-42). The recommendation for staging and target volume determinations is therefore PET-CT for lung cancer patients (7;43).

3.3.1. CT FOR RADIOTHERAPY

For accurate radiotherapy the anatomical structures in CT images must correspond to the fractionated conditions thoughout the individual treatment sessions. A conventional 3D-CT may be insufficient for thoracic cancer patients, as the 3D image can represent an arbitrary respiration phase. Respiratory motion could affect the CT images, representing an image of the extreme respiration phases such as the maximum inhalation or end-inhalation condition. A method to acquire CT images within motion is the respiratory-correlated 4D-CT technique.

Respiratory-correlated 4D acquisition monitors a patient's breathing using an external system such as Real-Time Position Management (RPM) from Varian Medical System. The RPM uses an infrared (IR) reflective marker box, located on the patient's chest to measure respiration. As the marker box moves according to respiration, an IR-detector acquire the vertical motion throughout the scan time. The collected RPM data for motion amplitude, phases and time stamps are retrospectively used to resample the CT slices into a collection of 3D-CT volumes (bins). This resampling of CT slices can be either amplitude- or phase-based. For amplitude binning, all CT slices within each bin contain volume data within the same amplitude window, whereas phase binning categorises the CT slices time resolved according to the respiration phase (25;44;45). By retrospectively sorting the images into a number of respiratory bins, the 4D-CT consists of multiple 3D-CT volumes, each presenting a narrow time or amplitude window of the respiration sequences. For radiotherapy, one of these bins is selected for treatment preparation depending on the treatment strategy. For respiratory-gated radiotherapy, the planning bin could represent the peak inspiration (often maximum distance to

OAR) or end-exhalation bin (most stable phase). For free breathing radiotherapy, a time average mid-ventilation phase may be selected to represent the most likely treatment position (46).

Even with the respiratory-correlated 4D-CT technique, image artefacts may exists that are caused by irregular respiration pattern, phase errors or residual motion blur (44;47-49). Variations in respiration patterns are typical described as changes in respiration cycle time or amplitude. Irregular respiration cycles could affect phase binning and lead to misinterpretation of tissue due to adjustment of the corresponding amplitude (24;50). On the other hand, though amplitude binning has been reported to be more reliable in terms of target position, it may not produce images at every respiration cycle due to a lack of amplitude levels. To ensure sufficient data collection in 4D-CT, the bin size, defined as the amplitude/phase window size, cannot be too small. On the other hand, a wide bin time allow for the occurrence of residual motions and potential image artefacts (47).

3.3.2. PET FOR RADIOTHERAPY

PET imaging using an FDG-tracer is a functional acquisition method to obtain an image of the metabolic activity in tissues. With FDG-tracer uptake as a metric for metabolic activity, variations in the uptake value allow tumour cells to be highlighted in PET scans (23;51). The PET image is acquired by integrating annihilation events as counts collected within a period of a few minutes. The events detected by the PET scanner are retrospectively reconstructed to a 2D or 3D image. Common reconstruction algorithms such as filtered backprojection or more recently iterative methods such as expectation maximization and time-of-flight corrections provide PET images with high contrast and reduced noise (52). The integration of PET and CT within identical reference conditions provide an essential image registration between the CT and PET volume. As for CT images in radiotherapy, the issue related to respiratory motion is also of concern in PET images. Within the period of PET acquisition, multiple respirations can lead to motion blur of the target lesion (22).
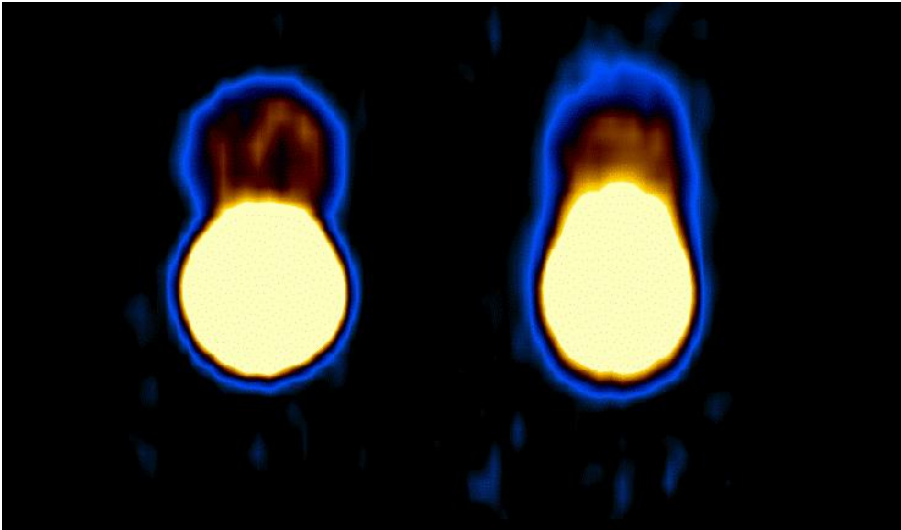
Figure 3. PET image of a FDG lesion with high tracer activity uptake in the bottom and low tracer activity uptake in the top. Left, a static PET scan with no motion during PET acquisition. Right, with 15mm motion amplitude throughout PET acquisition producing motion blur of the lesion.

The consequences can be a degradation of image gradients and uptake values depending on the target size and the lesion uptake ratio (53;54). For a 3D-PET scan, the lesion image would be time averaged, similar to the mid-ventilation CT phase from a 4D-CT. Alternatively a respiratory-correlated 4D-PET could be attained. Equivalent to the 4D-CT, a respiratory-correlated 4D-PET uses an external marker and a camera system to track and monitor respiration. For retrospective reconstruction of the different respiration bins, the PET scanner must acquire sufficient data (counts) to cover every bin. For a 2 minute PET acquisition in 3D mode, the time required for a 4D-PET would be a multiplication of the desired bins and acquisition time. Thus, the number of phase bins must be balanced between the needed time resolution and the uncertainties due to the extended scan time (55). Motion correction is another method to adjust 3D-PET images disturbed by respiratory motions (56;57). This method corrects 3D-PET images by either deblurring the PET image with a position probability estimate from 4D-CT or by modelling the respiration from two MRI images acquired at the inhalation/exhalation respiration phases.

For proper quantification of PET images, voxel intensity in terms of counts is commonly converted to standardized uptake value (SUV). The definition of SUV is the activity within a PET image in the time 't' relative to the body mass standardised injected activity (58).

$$SUV(t)\left[\tfrac{g}{ml}\right] = BodyWeight\ [g]\ \frac{Activity(t)\left[\tfrac{Bq}{ml}\right]}{injected_{activity}\ (t=0)[Bq]}$$ Eqn. 3.4

The SUV = 1 for a patient with uniform tracer distribution throughout the body volume. The SUV does not clearly distinguish malignant cells from healthy cells; thus, a target definition from a PET scan needs anatomical knowledge to separate healthy high SUV benign tissue from tumour cells. Different strategies have been investigated for accurate segmentation of cancers using both relative SUV and fixed thresholds. A percentage of the maximum SUV of 40-50% or a threshold including tissue with 2-3 times the SUV have provided tolerable segmentations for lung cancer target relative to CT segmentation (59-61). Recently, methods that are more sophisticated have been proposed using statistical or image gradient methodologies for PET segmentations (62;63). One such method from Geets et al. using gradient-based segmentation has provided accurate PET segmentations for both phantom targets and lung cancer specimens (63;64). However, for malignant tissue with various target shapes, tracer activity heterogeneity and motion during image acquisition hamper a straightforward clinical application.

A classification method to compare different PET acquisition techniques such as 3D, 4D and motion correction in combination with commonly used segmentation techniques is provided in Paper II.

3.1. IMAGE GUIDANCE

IGRT is a way of imaging- and focusing on the target position. Most IGRT techniques use KV imaging but other systems are available such as MV imaging and radiofrequency (RF) guidance for instance. Several vendors within the field of radiotherapy provide KV image guidance as cone-beam-computed-tomography (CBCT) or 2D X-ray images. The KV imaging technique is provided as an integrated application by vendors such as Varian Medical Systemt and Elekta Instruments or as add-on applications such as in the BrainLAB ExacTrac system. The Linac MV beam can handle image guidance, either as portal imaging or through MV tracking. For any instance, the images acquired for image guidance are successively registered to the planning CT or digitally reconstructed radiographs (DRR). When IGRT is influenced by respiratory motion, a short acquisition time with X-ray images may not necessarily correspond to the conditions in the planning CT. For free-breathing radiotherapy planned for the mid-ventilation CT phase, an X-ray image may relate to an arbitrary CT phase of a 4D-CT. For the instance of free breathing radiotherapy planned on the mid-ventilation CT phase, a CBCT acquired within multiple respirations may be sufficient. Alternatively, the image-guided X-ray acquisition could be synchronised to the respiration and acquired

within a corresponding respiration phase. Combined with radiotherapy beam control (gating), respiratory-gated IGRT may improve target localization (65).

3.1.1. GATING

Respiratory-gated radiotherapy facilitates radiotherapy according to predefined phases of the respiratory cycles. The RPM system from Varian monitors and tracks infrared-reflecting marker positions. The RPM system is coupled to image guidance through Varian On Board Imaging (OBI), enabling X-ray target monitoring inside the gating window. A comparable system is the BrainLAB ExacTrac, which uses five external infrared spheres located on the patient's chest to track respiration. The ExacTrac software supports both X-ray monitoring by bony anatomy or fiducials such as wires, seeds and stents.
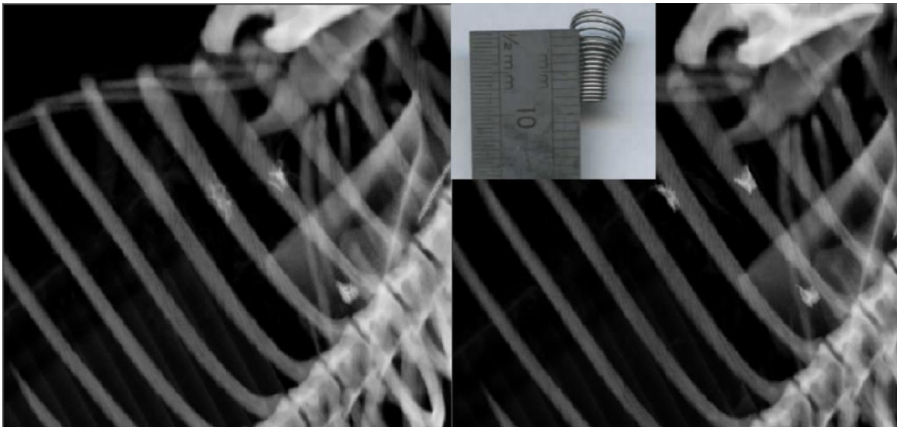
Figure 4. NiTi-stent positioned inside the bronchial airways for IGRT. Left image shows the mid-ventilation CT phase in which the fiducials appear blurred due to residual motion during CT phase acquisition. Right image illustrates a stable full exhale CT phase with nearly undistorted NiTi-stent visualization.

3.2. FIDUCIALS

The basic idea of having fiducials is a surrogate representation of a given organ or tissue. Fiducials may be implanted in the tissue for different purposes such as image registration or image guidance or tracking. For fiducial detection across multiple image modalities, image registration can be achieved by co-registering the fiducials. Even within mono-modal image modalities, the fiducials could be used for registration such as co-registration within low-contrast tissues or tracking of a moving target site. During the course of radiotherapy each session must correspond

to the planned target site with a minimal degree of uncertainty. Particularly for targets in low-contrast tissue, and a potentially moving thorax or abdominal targets. The fiducial should be located near the target and thereby act as a surrogate for the target position. For lung cancer fiducials, as gold marker (GM) seeds or wires are frequently used (66;67). Often, fiducials are inserted using a needle through the thorax wall and into the lung tissue near the target site. Some studies have reported complications such as pneumothorax and fiducial migration, related to the implantation (68;69). Another sort of fiducial is the nickel-titanium Stent (NiTi-stent) which has been tested within minipigs. The NiTi-stent is inserted through the bronchial airways with endoscopic equipment and has been shown to have a low rate of pneumothorax and migration (70;71). Most fiducials have high atomic Z-number which provides suitable contrast for image guidance with X-ray images such as CT, CBCT and 2D MV/KV-ray. Fiducials for image guidance may be designed specifically for the organ of interest and intended image modality within both treatment preparation and image-guided techniques (71;72).
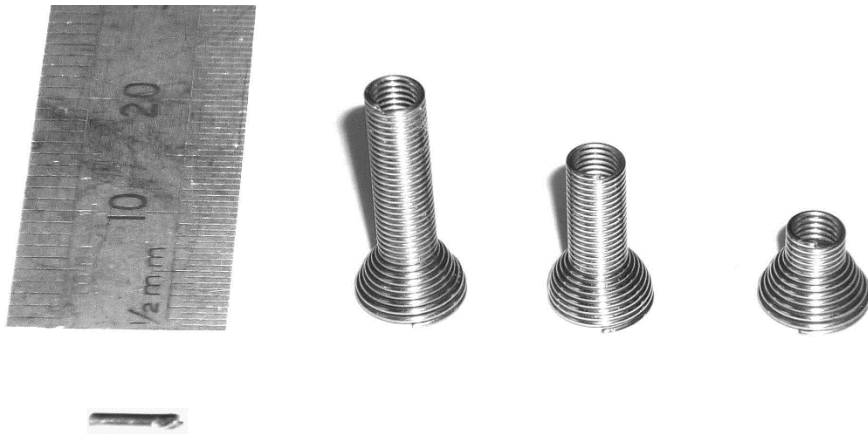
Figure 5. Fiducials intended as lung cancer surrogates; from left a GM seed (size 1 x 5 mm) and three NiTi-stents (length 15, 10 and 5 mm).

Due to residual motion during phase acquisition of a 4D-CT scan, the DRR used for image registration in IGRT may be distorted with potential additional margins for treatment planning. This might be of interest for non-gated radiotherapy using the mid-ventilation CT phase for treatment planning and image guidance.

Assessments of fiducial detection in respiratory-gated IGRT are described in Paper I. This work describes the uncertainties related to imaging of fiducials in both planning CT (4D-CT) and the subsequent detection for radiotherapy using gated image guidance.

3.3. IMAGE REGISTRATION

Image registrations in the field of radiotherapy are used for different purposes such as diagnostic images like CT, PET and MRI to IGRT in which anatomical structures or fiducials are registered in a planning CT. The principle of image registration is the determination of a unique spatial transformation of one image (moving image) into a reference image (fixed image). The most essential image registration procedure is the alignment of two images acquired under the same frame of reference condition. This could for instance be sequential CT scans or a hybrid PET/CT acquisition. Image registration within a unique frame of reference may be registered using a common DICOM origin. Alternatively, a rigid registration may be suitable in which solitary global shifts are valid. For images acquired within a period of weeks or months, a rigid registration may be insufficient due to tissue changes and patient misalignment.
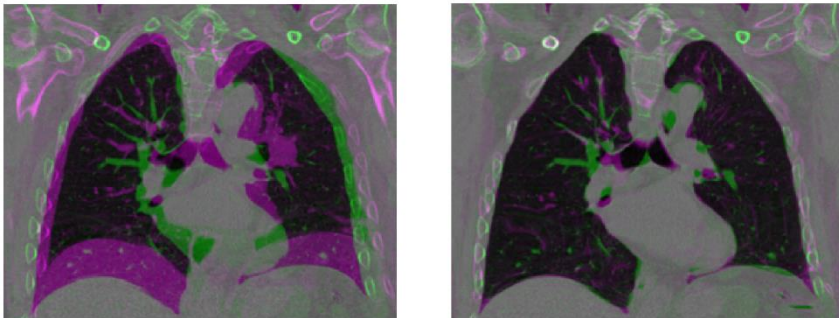
Figure 6. Rigid image registration (left) and (right) rigid image registration followed by deformable registration. In both images, the fixed reference image is visualised by green colour and the moving image as purple colour. Identical image intensities are visualised as grey-scale values.

For situations in which patient immobilization is unreliable and anatomical structures are likely to change, image registration methods with local deformable possibilities are preferred. Such methods, characterised as deformable image registration (DIR), are frequently used in medical image registrations (73;74). Different approaches have been suggested for performing DIR, such as the diffeomorphic Demon and spline methods (75;76). Generally, DIR methods are iterative methods that minimize image deviations. To perform image registration with an iterative method, a metric for similarities between the two images is

necessary. The similarity metric could be voxel intensity and intensity gradients or features such as distinct anatomical structures or corresponding sets of landmarks.

The preferred method for image registration depends on the purpose. For IGRT, a local registration method using a rigid transformation may be sufficient to ensure target site dose coverage. In this manner, an image registration volume of interest (VOI) could be limited to features near the target position or fiducials alone. For medical image registration such as dose planning quality assurance, adaptive dose planning or detection of anatomical changes, the VOI could be extended to include additional features. In those instances, the VOI could include any tissue inside the patient and thereby the entire image volume due to the focus on any anatomically structure. The distinct anatomical features need to either by identified by an operator or an atlas-based auto-contouring method. It may be a time consuming task to use manual user-defined image features, and some uncertainties are expected due to both observer and software variations (42;77).

For monomodal images registration such as CT co-registrations and X-ray image registration to CT for IGRT, voxel value similarities can be used. As such, a similarity metric for image registrations could be image intensity values or intensity gradients, and the user dependence may be limited. Widely used DIR methods for monomodal medical image registrations are the Demons and B-spline algorithms (73;74;76). The Demons algorithm maps the voxels of the registered moving image to the voxels of similar intensity within the static image, using the static image gradient to obtain the transformation direction. To avoid severe free form deformation with the Demons algorithm, constrains such as Gaussian smoothing or limitations to the transformation vector field could be applied. A parametric model such as the B-spline algorithm use spline functions to describe the deformations. A knot-point grid and the 'stiffness' of the polynomial upon which the spline functions are modelled can control the spline functions. Although DIR provide image registration with local alignments, previous studies evaluating DIR methods have noted the risk of unrealistic deformations (78;79). Hence, it is essential to have a strategy to validate DIR registrations that addresses both the uncertainties and locations of pitfalls associated with DIR.
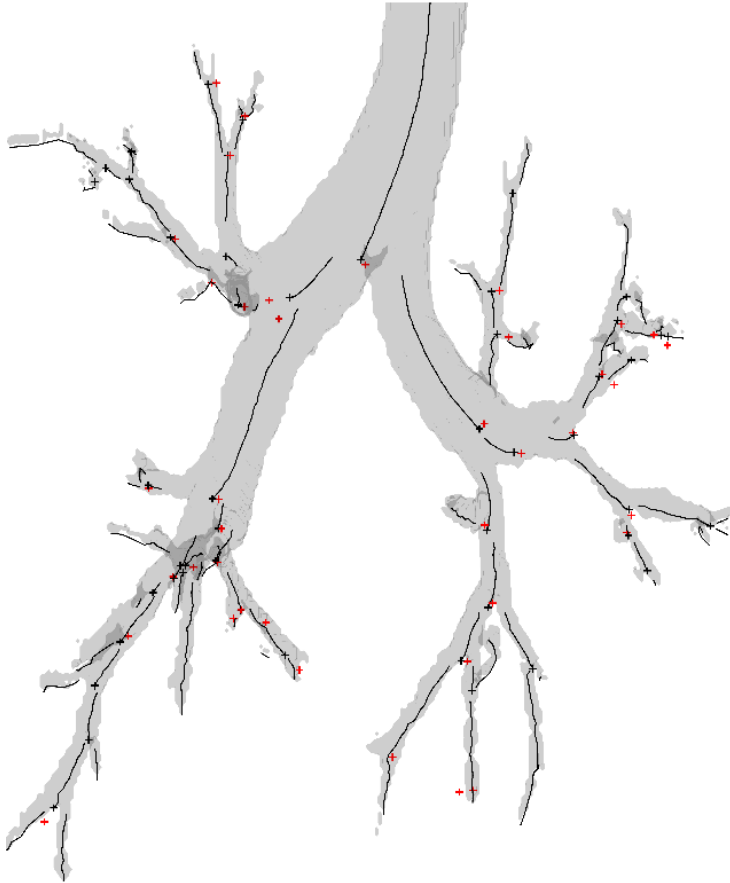
Figure 7. Anatomical feature in terms of airway segmentation with extracted bronchial branch point marked by black crosses. A red cross identifies a bronchial branch point within a registered image, and deviation between corresponding black and red crosses enables detection of local misalignment followed by image registration.

A method to validate DIR is provided in Paper III. The method uses extracted bronchial branch points from the segmented airways as anatomical features to validate the uncertainties of widely used DIR methods.

CHAPTER 4. THESIS OUTLINE

The thesis is divided into three main projects assessing uncertainties related to thoracic radiotherapy. The uncertainties in this thesis are restricted to the topic of fiducials in image guided radiotherapy, target segmentation in FDG-PET imaging and CT-CT image registrations.

The aims of the PhD thesis projects were to

- Assess detection accuracy of fiducials designed for thoracic radiotherapy in 4D-CT for treatment preparation and snap verification X-ray gated image guidance.

- Assess incorrect segmentations by semi-automatic PET segmentation methods for heterogeneous FDG-PET lesions affected by motion.

- Assess validation and identification methods for local registration disorders using a grid of automatically extracted anatomical landmarks.

CHAPTER 5. MATERIALS

A short description of the materials used in this PhD study are provided in the following section.

Study I was based on a phantom study with a standard BrainLAB Gating Phantom modified to provide equal and synchronized motion for both internal markers (fiducials) and external markers (Varian RPM Gating box or BrainLAB infrered reflecting spheres). The phantom motion was controlled using the BrainLAB Phantom controller with a custom sinusoidal motion of 20 mm, a cycle time of 4.9 sec and a latency time of 0.1 sec between cycles. An identical phantom setup was assembled at the Linac for gated IGRT X-ray verification images. The fiducials were located in a phantom slice with orientations in 0, 45 and 90 degree according to the scan and motion trajectory direction.

In study II, a Quasar respiratory motion phantom controlled the motion trajectory for PET acquisitions, with an amplitude of 15mm and a cycle time of 5.0 sec. The target lesions were mounted to the top of the phantom with a position near the phantom centre, which contained a uniform background tracer activity. For each tracer uptake ratio, PET_{sta}, PET_{4D}, and PET_{mot} scans were acquired successively, and residual FDG tracers were removed before cleaning the target lesions to avoid contaminations between scan setups.

Study III involved five previously diagnosed lymphoma patients. The CT data material consisted in low-dose CT scans acquired for diagnostic and follow-up PET/CT scans. All patients received chemotherapy in the period between the initial CT scans and the later scans, which were registered to the initial CT scan. None of the patients received radiotherapy in the periode of image acquisition used to validate image registrations.
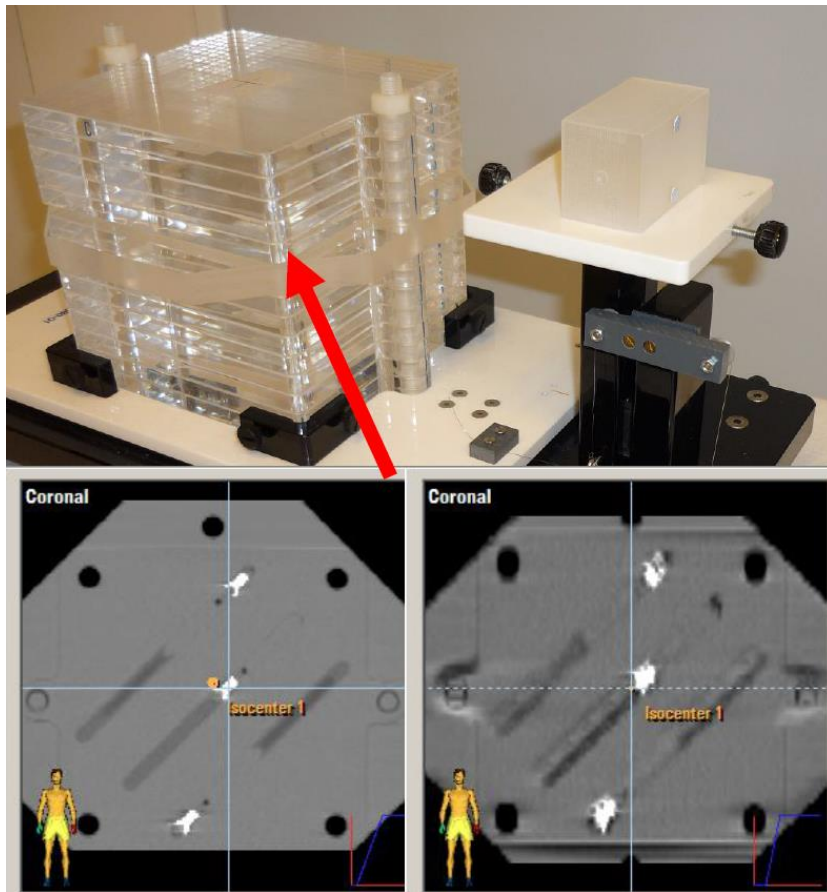
*Figure 8: The BrainLAB Gating Phantom used in study I with central plastic slice equipped
with fiducial markers. The illustrated fiducials (three 10mm NiTi stents) are visualized at 45°
in 4D-CT phase bin 50% (left) and 4D-CT phase bin 20% (right).*
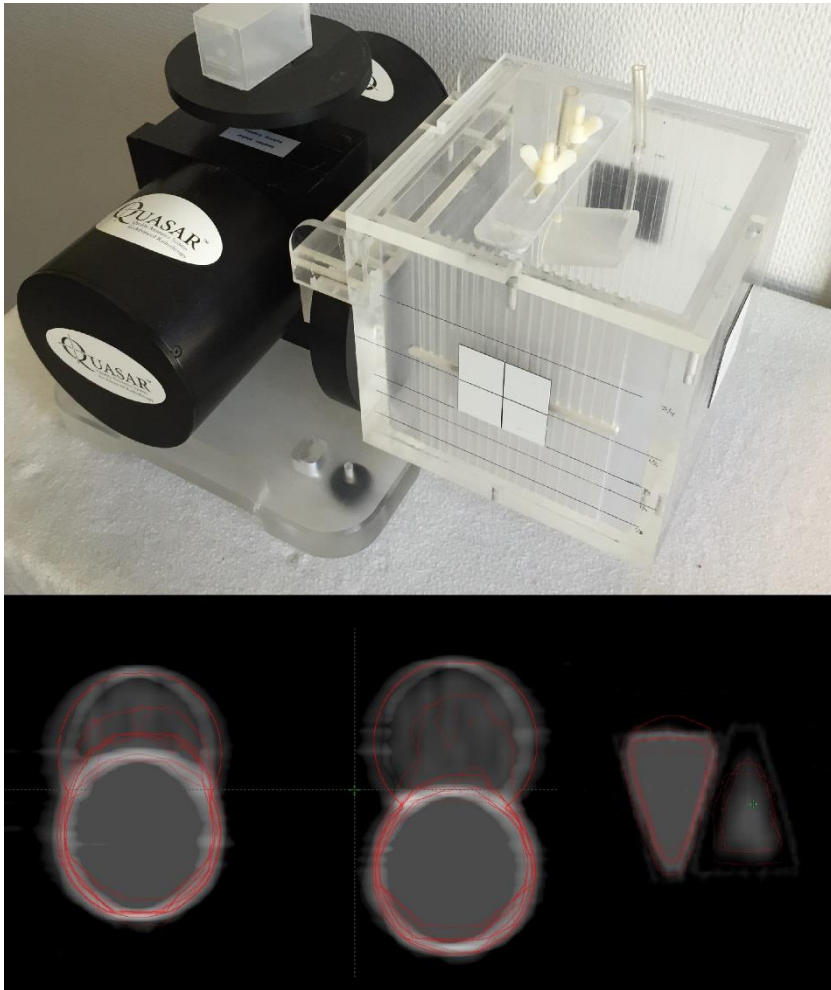
Figure 9:Modified Quasar respiratory phantom used in study II for PET imaging demonstrated in the top. Each of the three target lesions included a high- and a low FDG-tracer uptake sub-volume as illustrated in the bottom. The three demonstrated targets volumes are visualized using the FDG uptakeRatio of 4:2:1 with segmentations as red lines.

Patient	Sex/age	Primary disease	Bulky tumour	CT_1	CT_2
1	F / 61	Angioimmunoblastic T-cell lymphoma	None	3	10
2	M / 57	Diffuse large B-cell lymphoma	Jejenum	4	18
3	F / 52	Angioimmunoblastic T-cell lymphoma	None	5	9
4	M / 71	Diffuse large B-cell lymphoma	Delteoideus	3	5
5	M / 56	Morbus Hodgkin lymphoma	Kidney	5	10

Table 1: Patient summary with sex, age at the date of reference CT, primary disease and existence/location of a bulky tumour. Labels CT_1 & CT_1 specify time intervals in months from the reference CT to the subsequent CT acquisition used for image registration.

CHAPTER 6. RESULTS

A brief summary from each of the three papers is offered prior to each paper presentation.

Paper I

Potential position errors using fiducial markers for gated image guided radiotherapy

Nielsen MS, Nyström PMW, Carl J

This study aimed to quantify the detection uncertainties of fiducials designed for thoracic radiotherapy. The fiducials in this study were a gold marker seed and three different lengths of NiTi stents recently developed for implantations in the bronchial tree. The fiducials were positioned within a modified BrainLAB respiratory Gated phantom with synchronized internal (fiducials) and external (infrared reflecting spheres) simulation of respiratory motion. The fiducials were detected in 4D-CT and X-ray verification images for gated IGRT for different CT slice thicknesses, fiducial orientations and the different phases of the respiratory cycle. In 4D-CT, the detection uncertainties with standard deviations from 0.2 mm up to 2.2 mm were associated with fiducial speed at phase bin acquisition, fiducial orientation, and for the NiTi stent, the fiducial length. For gated IGRT, a systematic offset of 0.15 mm with a standard deviation of 0.6 mm was not associated with CT slice thickness, fiducial speed during image acquisition, orientation or fiducial type. In conclusion, detection uncertainties using fiducials for gated IGRT need an additional margin particularly for non-gated IGRT using the mid-ventilation phase for dose planning.

informa
healthcare

ORIGINAL ARTICLE

Potential position errors using fiducial markers for gated image guided radiotherapy

MARTIN S. NIELSEN[1], M. W. NYSTRÖM[2] & JESPER CARL[1]

[1]*Department of Medical Physics, Aalborg University Hospital, Denmark* and [2]*Department of Oncology, Uppsala University Hospital, Sweden*

Abstract
Background. Fiducials can be used as surrogate for target position during radiotherapy. However, fiducial motion could lead to potential position errors when using fiducials in four-dimensional computed tomography (4DCT) treatment planning and for gated image guided radiotherapy (IGRT). *Material and methods.* One gold marker (GM) and 5, 10 and 15 mm nickel-titanium (NiTi) stents were inserted in a moving phantom for the purpose of fiducial detection in 4DCT and gated IGRT. Fiducial position errors in 4DCT and BrainLAB's gated IGRT were defined as residuals between fiducial detection and the actual physical position at the instance of image acquisition. *Results.* Fiducials position errors correlate to speed, fiducial type and orientation during 4DCT acquisition. Lower detection accuracy was measured for the 5 mm NiTi-stent relative to the 10 and 15 mm NiTi stents and GM. Fiducials with orientation 45° relative to the scan direction showed a lower detection accuracy relative to parallel and perpendicular orientations. The standard deviation of position errors in 4DCT were up to 2.2 mm with a maximum deviation of 4.0 mm. Using BrainLAB's gated IGRT the fiducials were detected with a standard deviation of 0.6 mm and a maximum deviation of 1.9 mm. For gated IGRT no correlation to fiducial speed was found. *Conclusions.* Clinical use of fiducials in combination with treatment planning on mid-ventilation CT phase for moving target should include margins up to 5.5 mm due to potential systematic position errors.

One of the challenges in radiotherapy of thoracic cancer patients is the management of respiratory motion in both planning and treatment. One method for quantifying respiratory motion is four-dimensional computed tomography (4DCT) for treatment planning combined with gated image guided radiotherapy (gated IGRT). However, 4DCT does produce artefacts by irregularly respiration or lack of temporal resolution [1–3]. These uncertainties from the treatment preparation could lead to systematic errors, which calls for additional margin around the clinical target volume (CTV). A recent study [4] showed an increased risk of pneumonitis for inferior tumor positions, probably due to tumor motion and increased margin. IGRT could be one method to minimize the target margin. A variety of technical solutions have been developed for IGRT [5]. Some of the IGRT systems may furthermore be combined with respiratory management. Handling of respiratory motion requires observable and identical target definition on both planning CT and for IGRT. A recent study [6] comparing soft tissue and bone matching for lung tumors showed increased accuracy for soft tissue matching. Other surrogates visible in x-ray images are implanted fiducials such as gold marker seeds or wires (GM) [7,8]. An alternative fiducial could be insertion of intrabronchial nickel-titanium stent (NiTi-stent) recently tested on animals [9,10]. A study by Matney et al. [11] investigated the detection accuracy for a coil fiducial within 4DCT and for BrainLAB's gated IGRT system. However only one coil fiducial aligned parallel to the motion and a single slice thickness was investigated. Margin calculation according to van Herks formula [12] requires standard deviations of the systematic and random errors for clinical use.

The aim of this study is to quantify detection accuracies in terms of standard deviations within 4DCT and gated IGRT for different fiducials designed for thoracic cancer patients.

Correspondence: M. S. Nielsen, Department of Medical Physics, Aalborg University Hospital, Denmark. Tel: +45 9932 5148. Fax: +45 9932 2904. E-mail: martin.skovmos.nielsen@rn.dk

RIGHTS LINK

Material and methods

Fiducials and phantom

A GM sized 5 mm × 1 mm and NiTi-stents with different lengths of 5, 10 and 15 mm were used. The NiTi-stents had a diameter of 3.5 mm and a 6.0 mm expanded collar (Figure 1). Three identical fiducials were positioned in a solid plastic phantom for each experiment, separated laterally and longitudinally with a minimum distance of 40 mm. A standard BrainLAB ET Gating Phantom Ver1.0.0, manufactured by BrainLAB AG Feldkirchen Germany was used to simulate respiratory motion. It consists of two moving platforms, where one simulates an internal respiratory motion in the superior-inferior (S-I) direction, and the other simulates the external respiration (thoracic wall motion) in the anterior-posterior (AP) direction. The AP motion was used as a surrogate for the internal respiration during the 4DCT scans and the treatment simulation. For this study, synchronized motions between internal and external platforms were necessary as the external motion was used to define the physical phantom position during both 4DCT and gated IGRT. Consequently the two platforms were connected by a wire and driven by a single step motor. With synchronic platform motion, calibration of the phantom S-I motion amplitude was performed using the BrainLAB Infra-Red (IR) camera. Additionally, a reference AP motion curve was recorded as a mean motion path (SD = 0.1 mm, max deviation of 0.2 mm) within 2 min. The fiducial physical positions were defined relative to the AP reference curve. A nearly sine motion path with 20.0 mm amplitude and cycle time of 5.0 s was used. A motion closely related to a sine profile was selected to distribute phantom velocities almost equally between minimum and maximum values during the phase bin acquisitions.

Scan protocol

4DCT with 10 phase bins were acquired using a General Electric Medical Systems LightSpeed
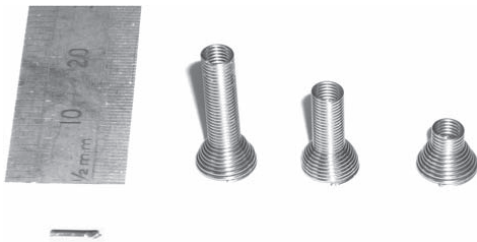
Figure 1. Fiducials used for evaluation of detection accuracies in 4DCT and gated IGRT. From left 5 mm Gold Marker seed, 15 mm NiTi-stent, 10 mm NiTi-stent and 5 mm NiTi-stent.

RT16 CT scanner with a GE workstation V4.2 and Varian RPM. 3D volumes were named according to the phase bin with CT phase bin 0% corresponding to maximum inhale and CT phase bin 50% to full exhale. The scanner was operated in cine axial mode at 120 kV and 80 mAs with a CT gantry rotation time and cine time between images of 0.5 s. Fiducials were scanned with slice thicknesses of 1.25 mm and 2.5 mm both with CT scanner collimation at 10 mm and axial resolution of 0.977 mm/pixels. While the phantom motion was only 1D with S-I displacement, the potentially fiducial orientation dependency was investigated. The NiTi-stents were scanned with orientations of 0°, 45° and 90° relative to the motion. The GMs were scanned with orientations 0° and 90° only.

Fiducials in each 4DCT scans were automatically detected using an in-house MatLab software script. All fiducials were segmented with a region growing method using the maximum pixel value within each slice as a seed point. The surrounding 26 voxels of the seed point were accepted by the segmentation algorithm according to the following two criteria: 1) A CT value above 1300 HU; and 2) A maximum distance threshold of 5 mm where clusters were accepted to merge a segmented volume. A CT value of 1300 HU was selected for two reasons. First, no phantom component contains CT values above 1300 HU except the electrical and mechanical parts. Second, all fiducials have CT value above 3072 HU (CT saturation value) in the stationary CT phases. Due to motion blur the CT values of the fiducials decrease in the non-stationary phases. Nevertheless fiducials were still detectable at 1300 HU. Ideally, this segmentation would provide three clusters, one for each of the three fiducials in the phantom. However, motion artefacts lead to fragments of segmented clusters. These fragments were handled by the second criteria, by which fragments were merging a segmented volume if the length of the 3D vectors between fragments were within the threshold of 5 mm. The non-fiducial parts (electric and mechanical) were excluded using a region of interest defined as the phantom surface.

Respiratory gated image guidance

Gated IGRT simulations were performed using a Varian Clinac iX equipped with BrainLAB ExacTrac Robotics V.5.52 and beam gating. The x-ray settings for image acquisitions were 100 kV, 50 mA and 100 mS. The acquired x-ray images were obtained at predefined amplitude levels according to Table I and during the exhale period only. The amplitude levels in Table I were selected to cover the phantom speed range during the time period from full inhale to end exhale. The fiducials were defined in the ExacTrac

Table I. Correlation between phantom speed values [mm/s], amplitude levels [%] for gated IGRT and phantom physical displacement [mm] relative to the initial setup with amplitude of 0 mm.

Speed [mm/s]	Amplitude [%]	Displacement [mm]
3.1	3.0	0.6
7.0	10.0	2.0
11.9	25.0	5.0
14.6	50.0	10.0
13.2	75.0	15.0
9.6	90.0	18.0
4.3	98.0	19.6

Figure 2. Fiducials center-of-masses within the 4DCT normalized to phase bin 50%. The figure represents all fiducials, slice thicknesses and orientations. The solid line indicates the actual physical position of the fiducials within a full cycle.

software using endpoint description for fiducials of type 10 mm and 15 mm NiTi-stents. The GM and the 5 mm NiTi-stent were defined using a single point as these fiducials were displayed on a few number of CT slices. The BrainLAB gating module operates with relative amplitude values (0–100%) as described in Table I. Initially, the phantom was positioned with an amplitude level of 0% identical to CT phase bin 50%. With motion applied to the phantom, the fiducials were moving with a displacement of 20 mm relative to the initial setup. Accuracies of the gated IGRT were calculated as residuals between the fiducial positions detected on gated verification images and the expected physical displacement from the initial setup.

Results

4DCT

Three segmented volumes were achieved within all 4DCT scans using the region growing method. A total of 66 fiducial volumes were segmented for each phase bin, using the combination of three fiducials in each scan, four different fiducials, two slice thicknesses and three orientations (two orientations for GM). All the fiducial center-of-masses detected in retrospectively sorted CT phases were plotted in Figure 2. No deviation occurs at phase bin 50% as this phase was used as reference for the entire positioning measurements. Segmented position errors were within 0.2 mm in the AP and left-right directions. The maximum fiducial deviation from the reference position was 4.0 mm. A summary of fiducial detected position errors in 4DCT is listed in Table II. F-tests for equal variances were used to separate position errors between fiducial types, orientations and slice thicknesses. No differences in position errors between the CT slice thicknesses of 1.25 mm and 2.50 mm were observed (p = 0.85). The standard deviations of position errors were correlated to the phantom speed at each phase bin center. In Figure 3 the standard deviations are plotted for each fiducial type and in Figure 4 according to fiducial orientations. Linear regression on the former data confirmed a significant different slope for the 5 mm
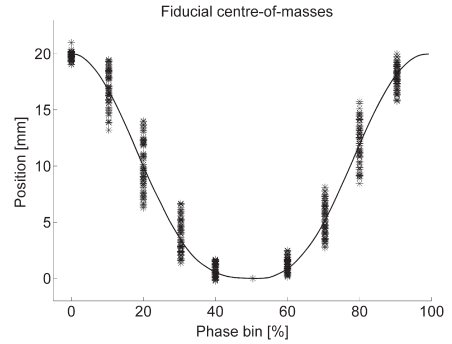
NiTi-stent (p = 0.003) compared to the GM, 10 and 15 mm NiTi-stent which have identical parameters. The linear regression for fiducial orientations (all fiducials included) confirmed a significant different slope for fiducial aligned at 45° relative to phantom motion (p = 0.006).

The interception points of the linear regression for fiducial types and orientations, respectively, showed no significant variation, corresponding to identical position errors on CT phases acquired at low speed. The standard deviation of fiducial position errors were in the range of 0.2 mm to 2.2 mm, using regression parameters for fiducials with 45° orientation only.

BrainLAB's gated IGRT

A total of 44 fiducial detections were performed at each phantom speed level in Table I. Two sets of verification images were acquired for each of the four fiducial types, two slice thicknesses and three orientations (GM two orientations). The standard deviations for verification images showed no significant differences across phantom speed values. The maximum fiducial detection from the expected position was 1.9 mm. For the gated IGRT no correlation was found to fiducial type, orientation and slice thickness. In this study fiducial position with BrainLAB's ExacTrac gated image guidance was verified with a mean deviation from the physical position of 0.15 mm CI (0.06; 0.24). The standard deviation of the total distribution of position errors was 0.63 mm. Using one-sample T-test points to an offset of the mean value from zero (p = 0.0008).

Discussion

The distributions of the segmented fiducials agreed with the actual physical positions within 4DCT, as the

Table II. 4DCT fiducial detection divided into groups of fiducial types, orientations and CT scan slice thicknesses. The fiducial position errors were listed with mean residuals over all CT phases and both slice thicknesses and the 95% CI of the mean and standard deviation (SD) of the group distributions. The mean of fiducial types were for all orientations and both slice thicknesses. Similarly the mean of fiducial orientations were for all types and both slice thicknesses. The mean of slice thicknesses were for all fiducials and orientations. Regression parameters for the standard deviations were listed with 95% CI for fiducial types and orientations with both slice thicknesses included.

Group	Mean [mm]	SD [mm]	Regression slope [mm/s]	Regression intercept [mm]
Fiducial type				
15 mm stent	0.06 [−0.13; 0.27]	1.29	0.11 [0.09; 0.12]	0.16 [0.05; 0.27]
10 mm stent	0.05 [−0.13; 0.24]	1.21	0.11 [0.09; 0.12]	0.16 [0.05; 0.27]
5 mm stent	0.23 [−0.04; 0.50]	1.73	0.16 [0.13; 0.19]	0.13 [−0.16; 0.42]
5 mm GM	0.19 [−0.04; 0.41]	1.19	0.11 [0.09; 0.12]	0.16 [0.05; 0.27]
Fiducial orientation				
0°	0.17 [−0.01; 0.34]	1.30	0.11 [0.09; 0.12]	0.16 [0.01; 0.30]
45°	0.15 [−0.10; 0.39]	1.57	0.15 [0.13; 0.16]	0.14 [−0.03; 0.31]
90°	0.07 [−0.10; 0.25]	1.33	0.11 [0.09; 0.12]	0.16 [0.01; 0.30]
CT slice thickness				
1.25 mm	0.12 [−0.04; 0.28]	1.38	–	–
2.50 mm	0.14 [−0.02; 0.30]	1.40	–	–

mean and 95% CI in Table II were close to zero. However, by separating the position errors into different speed regimes during the 4DCT some differences could be observed. The lower accuracy of the 5 mm NiTi-stent position is likely to be a combination of a small size and less dense material (NiTi). This could affect the segmented volume and thus the center-of-mass in CT phases acquired at high speed. Similarly, less accuracy for fiducials with 45° orientation was observed. An exact alignment of fiducials during implantation parallel or perpendicular to the motion is not feasible in a clinical situation. Therefore, the safety margin for fiducials should be considered from position errors on fiducials aligned at 45°, which in this study ranged from 0.2 mm to 2.2 mm. Applying a systematic deviation of 2.2 mm into Van Herks

formula [12] for margin calculation, results in a CTV margin of 5.5 mm due to position uncertainty. The maximum speed value in this study was closely related to the time weighted mid-ventilation phase. The mid-ventilation phase is frequently used for dose calculation in radiotherapy [13–15]. Thus, calculated CTV margin in this study may be clinically relevant for a target in the inferior thorax where 20 mm motion [1] has been observed. Alternatively using the 4DCT exhale phase for dose calculation, the CTV margin due to fiducial position uncertainty can be reduced to 0.5 mm, because of the minimal motion during phase bin acquisition. Even though GMs were only segmented on one or two slices with orientation at 90°, the slice thicknesses showed not to influence the fiducial precision. Using the center-of-mass instead of full

Figure 3. 4DCT standard deviations of the fiducial position errors relative to phantom speed at center of phase bin acquisition. All three orientations and both slice thicknesses were included with separation into groups of fiducial types. Linear regression for the 5 mm NiTi stent were significant different from the other three fiducials (Table II).
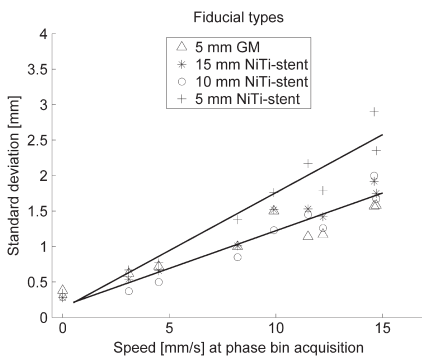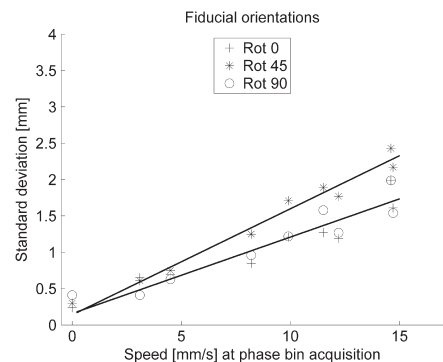

Figure 4. 4DCT standard deviations of the fiducial position errors relative to phantom speed at center of phase bin acquisition. All fiducial types were included with both slice thicknesses with separation into fiducial orientations. Linear regression for fiducial orientated at 45° were significant different from the other two orientations (Table II).

length as fiducial detection may have blurred the distribution within equal variances.

The position accuracy of the BrainLAB gated IGRT system shows no correlation to motion speed during image acquisition. The lack of correlation to phantom speed may be related to the rapid x-ray verification time of 100 ms. During this time the phantom moves up to 1.5 mm which is not far from the measured 95% prediction interval of 1.2 mm (two standard deviations for position errors). BrainLAB's gating system uses IR markers on the phantom to predict the respiratory motion, combined with two X-ray images which are not acquired synchronically in one respiration cycle. The precision of this system is consequently linked to its ability to acquire two sequential X-ray images at reproducible amplitudes during respiration. This, however, does not constitute a problem in the current study, as the respiratory motion is close to sine shaped and identical within repeated cycles. Irregular patient respirations would probably influence the tracking precision which was not investigated in this study. Our study showed a systematic position error of 0.15 mm (mean deviation from expected position) for gated IGRT. This indicates that x-ray images were acquired slightly before time. Results in this study are in accordance with Matney et al. [11] who used a coil fiducial and reported a maximum position deviation up to 3.5 mm in 4DCT and less than a millimeter using BrainLAB gated IGRT. Matney et al. also found the largest position deviations occurred in CT phases with the highest velocities. In contrast to the present study, Matney et al. only measured for a coil fiducial aligned parallel to phantom motion and thus not correcting for the effects of a fiducial rotation. The group only reported maximum deviations and did not provide an error estimate for the clinical situation. The maximum deviation of a single detected fiducial center-of-mass in our study was 4.0 mm on 4DCT and 1.9 mm for the gated IGRT.

In conclusion accuracy of fiducial position in 4DCT demonstrated correlation to fiducial orientation, material density/size and speed during the CT phase selected for treatment planning. These effects may have to be included in the CTV to planning target volume margin in case of radiotherapy for respiratory moving targets.

Acknowledgements

References

[1] Keall PJ, Mageras GS, Balter JM, Emery RS, Forster KM, Jiang SB, et al. The management of respiratory motion in radiation oncology report of AAPM Task Group 76. Med Phys 2006;33:3874–900.

[2] Persson GF, Nygaard DE, Brink C, Jahn JW, Munck Af RP, Specht L, et al. Deviations in delineated GTV caused by artefacts in 4DCT. Radiother Oncol 2010;96:61–6.

[3] Persson GF, Nygaard DE, Af Rosenschold PM, Richter V, I, Josipovic M, Specht L, et al. Artifacts in conventional computed tomography (CT) and free breathing four-dimensional CT induce uncertainty in gross tumor volume determination. Int J Radiat Oncol Biol Phys 2011;80:1573–80.

[4] Vogelius IR, Bentzen SM. A literature-based meta-analysis of clinical risk factors for development of radiation induced pneumonitis. Acta Oncol 2012;51:975–83.

[5] Verellen D, De RM, Storme G. A (short) history of image-guided radiotherapy. Radiother Oncol 2008;86:4–13.

[6] Josipovic M, Persson GF, Logadottir A, Smulders B, Westmann G, Bangsgaard JP. Translational and rotational intra- and inter-fractional errors in patient and target position during a short course of frameless stereotactic body radiotherapy. Acta Oncol 2012;51:610–7.

[7] Bhagat N, Fidelman N, Durack JC, Collins J, Gordon RL, LaBerge JM, et al. Complications associated with the percutaneous insertion of fiducial markers in the thorax. Cardiovasc Intervent Radiol 2010;33:1186–91.

[8] Yousefi S, Collins BT, Reichner CA, Anderson ED, Jamis-Dow C, Gagnon G, et al. Complications of thoracic computed tomography-guided fiducial placement for the purpose of stereotactic body radiation therapy. Clin Lung Cancer 2007;8:252–6.

[9] Carl J, Nielsen J, Nielsen MS, Zepernick PR, Kjaergaard B, Jensen HK. A new lung stent tested as fiducial marker in a porcine model. Radiother Oncol 2012;102:297–302.

[10] Carl J, Jensen HK, Nielsen J, Nielsen MS, Schmid M, Siegfried L. A new fiducial marker for gated radiotherapy in the lung – a feasibility study of bronchoscopy based insertion and removal in Göttingen mini-pig. Scand J Lab Animal Sci 2010;37:117–27.

[11] Matney JE, Parker BC, Neck DW, Henkelmann G, Rosen II. Target localization accuracy in a respiratory phantom using BrainLAB ExacTrac and 4DCT imaging. J Appl Clin Med Phys 2011;12:3296.

[12] van Herk M, Remeijer P, Rasch C, Lebesque JV. The probability of correct target dosage: Dose-population histograms for deriving treatment margins in radiotherapy. Int J Radiat Oncol Biol Phys 2000;47:1121–35.

[13] Wolthaus JW, Schneider C, Sonke JJ, van HM, Belderbos JS, Rossi MM, et al. Mid-ventilation CT scan construction from four-dimensional respiration-correlated CT scans for radiotherapy planning of lung cancer patients. Int J Radiat Oncol Biol Phys 2006;65:1560–71.

[14] Korreman S, Persson G, Nygaard D, Brink C, Juhler-Nottrup T. Respiration-correlated image guidance is the most important radiotherapy motion management strategy for most lung cancer patients. Int J Radiat Oncol Biol Phys 2012;83:1338–43.

[15] Li G, Citrin D, Camphausen K, Mueller B, Burman C, Mychalczak B, et al. Advances in 4D medical imaging and 4D radiation therapy. Technol Cancer Res Treat 2008;7:67–81.

Paper II

PET segmentation of thoracic lesions – is 4D PET necessary?
Nielsen MS, Carl J

Submitted to Jounal of Nuclear Medicine

PET imaging using radioactive tracers such as FDG provides reduced SUV when exposed to motion during image acquisition. Consequently, degraded SUV can lead to misinterpretation of target lesions for diagnostic purposes. The aim of this study was to assess the differences between common segmentation methods for targeting heterogeneous lesions influenced by motion during image acquisition. Three target shapes with dual tracer activity levels (high- and low-uptake) were segmented using four commonly used semi-automatic segmentation methods using 4D-PET, motion-included 3D-PET and motion-corrected 3D-PET. Target segmentations were compared to similar targets of images acquired in static 3D-PET using volume differences (ΔVol) and an error estimate for low-uptake volume (lowUptake$_{error}$). In 4D-PET, segmentations were close to static imaging conditions. For motion-included 3D-PET images, a significant overestimation was observed using the GradientSeg method. No significant segmentation variations were observed for the SUV40% and 2.5SUV methods in motion-included 3D-PET images. The Max40% presented a lowUptake$_{error}$ equal to static segmentation, whereas the ΔVol exposed overestimation of the segmented volume. Equal segmentations in motion-corrected 3D-PET images compared to static 3D-PET was exclusively presented with the GradientSeg method. FDG lesions with heterogeneous tracer activity revealed dissimilarities for commonly used segmentation methods, with GradientSeg being the most consistent method in motion-corrected PET images.

PET segmentation of thoracic lesions – is 4D PET necessary?

Martin S. Nielsen[1], Jesper Carl[2]

[1] Department of Medical Physics, Aalborg University Hospital
[2] Department of Clinical Medicine, Aalborg University

Keywords:
FDG PET segmentation - lung cancer

Corresponding author:
Martin Skovmos Nielsen
Department of Medical Physics
Aalborg University Hospital
Hobrovej 18-22
9000 Aalborg
Denmark
Email: martin.skovmos.nielsen@rn.dk

Abstract

Respiratory-induced motions of the thorax are prone to degrade the Positron Emission Tomography (PET) signal with the consequent loss of image information and unreliable segmentations. This study aims to assess the discrepancies of widely used semi-automatic PET segmentation methods for lung cancer on heterogeneous target lesions influenced by motion during image acquisition. **Methods:** Three target lesions included dual F-18 Fluoro-deoxy-glucose (FDG) tracer concentrations as high- and low FDG activities relative to the background. Four different tracer concentration arrangements were segmented using three SUV threshold methods and a single gradient based method. Static 3D-PET scans (PET_{sta}) designed the reference segmentation conditions for the individual segmentation methods, target lesions and tracer concentrations. For motions involving PET scans, a 15 mm amplitude of a nearly sinusoidal superior-inferior displacement was applied to the phantom within 4D-PET (PET_{4D}) and 3D-PET (PET_{mot}) scanning protocols. Motion-corrected images (PET_{deb}) using position density estimates derived from 4D-CT images were additionally extracted from the 3D-PET motion-included images. Segmentations in PET_{4D}, PET_{mot} and PET_{deb} were compared to the corresponding segmentations in PET_{sta} images according to volume changes (ΔVol) and an error estimate ($lowUptake_{error}$) for the lesion part covering the low tracer concentration. **Results:** In the 4D-PET image, the segmentation methods all provided $lowUptake_{error}$ estimates equivalent to PET_{sta} segmentations and, except for the Max40% segmentations, a slight volume expansion. In the PET_{mot} images, the GradientSeg method results in an average 43 % increased volume and an overestimation of 0.33 for the $lowUptake_{error}$. The 2.5SUV and SUV40% methods both provided segmentations in PET_{mot} images equivalent to PET_{sta} segmentations according to both ΔVol and the $lowUptake_{error}$ quantity. The Max40% significantly overestimated the volume whereas the $lowUptake_{error}$ was equivalent to PET_{sta} segmentations. In the PET_{deb} images, the GradientSeg was the only method to provide equivalent segmentations as in PET_{sta} images for both ΔVol and $lowUptake_{error}$. **Conclusion:** The use of FDG with various tracer concentrations revealed according to PET_{sta} images that the most consistent segmentations for motion-corrected PET images (PET_{4D} or PET_{deb}) were achieved using the GradientSeg method.

Introduction

In general, lung cancer is classified into two main categories, defined as Small Cell Lung Cancer (SCLC) and Non-Small Cell Lung Cancer (NSCLC). The majority and minority of all lung cancers are classified as NSCLC (85 %) and SCLC (15 %) respectively (1;2). For both SCLC and the NSCLC, radiotherapy is one treatment strategy depending of the extent of the cancer as indicated by lymph node involvement and potential metastases according to the TNM definition (3). The hybrid Positron Emission Tomography (PET) and Computed Tomography (CT) and recently introduced PET and Magnetic Resonance Imaging (MRI) scanners benefits a minimal misrepresentation between image acquisitions (4;5). The combined use of F-18 Fluoro-deoxy-glucose (FDG) PET and CT provide high accuracy for the clinical staging of lung cancers (6-8) and lower inter-observer variation for target definition (9). A high FDG uptake was associated with the preferential site of local relapse of NSCLC in a recent study by Calais et al (10). Respiratory motion may result in motion artefacts, thus requiring image correction of motions in a PET/CT scan (4D-PET/CT). The 4D-PET/CT scan benefits by nearly motion free images by selecting an appropriate number of respiratory phase bins and thus, it may further improve cancer staging and target volume definition in radiotherapy (11). The use of semi-automatic delineation (segmentation) methods may reduce the inter-observer variation in the Clinical Target Volume (CTV) outline for radiotherapy (12;13). Some PET segmentation methods for outlining CTV are intensity-based, such as the Standard Uptake Value (SUV) or the fixed/adaptive threshold activity value. Other more sophisticated methods may be established using activity statistics, resulting in segmented clusters or the use of spatial gradients in activity for segmenting boundaries (14;15). Currently, no consensus exists on methods for FDG-PET segmentation in lung cancer, but a threshold of 2.5 SUV or a percentage of the maximum SUV (SUV_{max}) such as 40-50% is widely used (7;8;16). Using a fixed SUV threshold for target determination still result in variations in target definition due to partial volume effect, activity recovery and FDG uptake heterogeneities (17;18). For PET/CT imaging of lung cancer, the effect of respiratory motion may additionally result in image intensity changes or eroded intensity gradients. Consequently, respiratory motion could result in less accuracy in established segmentation methods and therefore in uncertainty of CTV definition.

The main purpose of this work was to construct various in-house phantoms with heterogeneous PET tracer activities and to study the effect of motion on commonly used semi-automatic PET segmentation methods. A secondary purpose was to study the effect of commonly used segmentation methods on post-processed motion corrected 3D-PET images created by the deconvolution of motion involved 3D-PET images with target position density derived from a 4D-CT scan.

Materials and methods

The target volumes consisted of three in-house manufactured interlaced double volumes, titled A, B and C submerged in a water-filled phantom of size 17 cm x 17 cm x 18 cm (Figure 1). Each of the three target volumes involved high and low PET tracer uptake sub-volumes (highUptake = A1, B1 & C1 and lowUptake = A2, B2 & C2), allowing for different PET tracer uptake ratios relative to a uniform background activity. The water-filled phantom with target volumes was connected to a QUASAR^{TM} Respiratory Motion Phantom (ModusQA Medical Devices). In static mode, no motion was applied to the phantom, whereas in motion mode, a 15 mm peak-to-peak amplitude (nearly sine profile), 15 cycles per minute, orientated in the scanner longitudinal z-direction was applied to the phantom.

A total FDG PET tracer activity of 80-120 MBq (Injected$_{activity}$) was prepared for the phantom with four different FDG concentrations (ratios) relative to the background activity of SUV = 1. The SUV definition for this study was corrected for FDG activity decade at acquisition time (t) as the following:

$$SUV = Phantom_{weight}[g] \frac{Voxel_{activity}(t)\left[\frac{Bq}{ml}\right]}{Injected_{activity}(t)[Bq]} \tag{1}$$

with Phantom$_{weight}$ defined as background water and target volume materials.

The target volume uptake ratios (uptakeRatio) were organized as 4:4:1, 3:2:1, 4:2:1 and 8:3:1, where for instance, a ratio of 4:2:1 represented a highUptake SUV = 4, a lowUptake SUV = 2 and a background SUV = 1. The ratio of 4:4:1 indicated equal uptake (SUV = 4) for both high- and lowUptake sub-volumes. The highUptake sub-volumes (A1, B1 & C1) were included in every PET segmentations, whereas the lowUptake sub-volumes (A2, B2 & C2) were estimated to be segmented in approximately half of the uptake ratios as labelled in Table 1.

For each instance of FDG uptake ratio, the individual target volumes were subjected to scan protocols in both static- and motion- modes using an integrated PET/CT scanner (Discovery STE, GE Healthcare).

Static mode:

3D-CT (CT$_{sta}$). Acquired in helical mode at 120 kVp, 80 mAs. The CT scan length was marginally beyond the water-filled phantom volume of 17 cm plus the respiratory motion extent.

3D-PET (PET$_{sta}$). Acquired using a 2 min acquisition time for a single bed position, equivalent to a single bin in the 4D-PET.

Motion mode:

3D-PET (PET$_{mot}$). Acquired using a 2 min acquisition time for a single bed position equivalent the PET$_{sta}$ protocol. A corresponding CT in motion mode was acquired equivalent to the CT$_{sta}$ protocol.

4D-CT (CT$_{4D}$). Acquired in the cine axial mode at 120kV, 80mAs with the CT gantry rotation time at 0.5 sec, cine time between images of 0.5 sec and a total cine duration of 5 sec. The 4D-CT was retrospectively re-

sorted into 6 phase bins (maximum phase error 5 %), using respiratory motion data obtained by the Real-time Position Management System (RPM from Varian Medical System).

4D-PET (PET$_{4D}$). Acquired using a total PET acquisition time of 12 min, for 6 PET bins (2 min per phase bin). The number of phase bin was carefully chosen to obtain nearly motion free PET images. Given the motion amplitude and target size, Bettinardi et. al proposed the number of bins to obtain motion-free images in 4D-PET according to motion-amplitude and target sizes (11).

The CT scans were reconstructed with a CT slice thickness of 1.25 mm and a matrix size of 512x512 pixels (voxel size 0.977 x 0.977 x 1.25 mm^3). The PET scans were acquired in 3D mode and reconstructed to a matrix size 256 x 256 x 47 pixels (voxel size 2.73 x 2.73 x 3.27 mm^3) with the 3D-OSEM algorithm (2 iterations, 26 subsets) and a post-Gaussian filter of 3 mm full-width-half-maximum. The corresponding 4D-CT (matching CT phase bin) or 3D-CT were used for attenuation correction of the PET images.

In addition, a motion corrected post-processing procedure (motion deblurring) applied to the PET$_{mot}$ scans resulted in PET images labelled PET$_{deb}$. The following section provides a more detailed description of the motion-correction procedure.

Motion-correction:

The motion-corrected PET$_{deb}$ were iteratively reconstructed from the PET$_{mot}$, comparable to the work by Naqa et. al (19). The PET$_{deb}$ volumes were derived by deconvolving PET$_{mot}$ with a target position probability kernel (K$_{motion}$), estimated from the 4D-CT. The K$_{motion}$ was derived using a normalized position probability kernel estimated from the CT target centre-of-mass position within the 4D-CT. Using the phantom trajectory of motion aligned in the superior-inferior (z-axis), the main contribution to the position probability density was coupled to this direction. The 4D-CT acquired with the same FDG uptake ratio was used for the K$_{motion}$ determination using a rigid target propagation from the CT phase bin 0 % throughout the remaining five phases. A forward Van-Cittert iterative deconvolution method was performed as following:

$$PET_{deb}^{k+1} = PET_{deb}^{k} + \left[PET_{mot} - PET_{deb}^{k} \otimes K_{motion} \right] \qquad (2)$$

with the initial condition $PET_{deb}^{k=0} = PET_{mot}$. For simplification, the deconvolution was implemented in 2D space, and the PET$_{mot}$ was thus resliced within the primary 2D motion plane (x,z). Succeeding each iteration a post-processing image correction was applied, limit the PET_{deb}^{k+1} within the original PET$_{mot}$ minimum and maximum values within a 4 mm radius, thereby reducing Gibb's phenomenon.

The individual PET and corresponding CT scans were co-registered using a common frame of reference (DICOM origin). A chain of PET registrations were organized as registration from PET$_{sta}$ to the mid-ventilation PET$_{4D}$ (bin3) and PET$_{4D}$ (bin3) to PET$_{mot}$ and PET$_{deb}$ using full range PET intensity registration for a volume of interest covering lesions with a roughly 2 cm isotropic margin.

Segmentation:

Four different PET segmentation methods were applied to the PET images, PET$_{4D}$, PET$_{sta}$, PET$_{mot}$ and PET$_{deb}$ for each of the three experimental phantom volumes A-C.

I. Max40%: A fixed threshold at 40% of the maximum SUV value defined as the mean SUV over 1 cm^2 around the peak intensity pixel. Voxels above the threshold value were segmented as the target volume.

II. SUV40%: Threshold of 40% maximum SUV as described above and corrected for the background level (SUV$_{bg}$). The segmentation included voxels beyond the threshold value defined as

$$SUV40\% = 0.40\ (SUV_{max} - SUV_{bg}) + SUV_{bg} \tag{3}$$

III. GradientSeg: Gradient-based watershed segmentation. A segmentation process developed by Geets et.al (15), named IMREviewer. Segmentation with IMREviewer presented robust accuracy for lung cancer, in comparison with surgical specimens (7;20). The IMREviewer prepared the PET images by initially denoising and later deblurring with the PET scanner FWHM (5.4 mm) kernel, defined by a Gaussian approximation to a point spread function measured for the scanner central axis.

IV. 2.5 SUV: Threshold of 2.5 times the Standardize Uptake Volume (SUV). The segmentation included voxels with an uptake value above 2.5 SUV.

For the static CT (CT$_{sta}$) images, the high- ($CT_{highUptake}$) and lowUptake ($CT_{lowUptake}$) sub-volumes were segmented separately. For targets A and B, a 3D-sphere of 39 mm (internal sphere diameter) was used as the geometric 3D structure for segmentations followed by Boolean operation to separate CT$_{highUptake}$ and CT$_{lowUptake}$. For the cone shaped target C, the first and last CT slice containing the target was segmented as 2D planar circles (diameter of 7 and 27 mm) followed by linear interpolation.

Data analysis:

The PET segmented volumes in the different scan protocols (SEG$_{4D,mot,deb}$) were compared to the static segmentations (SEG$_{sta}$) according to volume change (ΔVol) and an error estimate of the lowUptake sub-volume (lowUptake$_{error}$) for each segmentation method.

The segmented volume change was defined as the difference between PET segmentation relative to static segmentation for an equivalent segmentation method, target and tracer uptakeRatio.

$$\Delta Vol\ = \frac{SEG_{sta,4D,mot,deb}[cm3] - SEG_{sta}[cm3]}{SEG_{sta}[cm3]} \tag{4}$$

The lowUptake$_{error}$ was defined by the volume similarity as the Dice Similarity Coefficient (DSC) between PET segmentations and the CT$_{lowUptake}$ volumes labelled A2, B2 and C2 in Figure 1.

I. $DSC_{lowUptake}$ as spatial volume similarity between the PET segmented volume and the $CT_{lowUptake}$ for the specific segmentation methods, target and uptakeRatio.

$$DSC_{lowUptake}^{sta,4D,mot,deb} = \frac{2|SEG_{sta,4D,mot,deb} \cap CT_{lowUptake}|}{|SEG_{sta,4D,mot,deb}| + |CT_{lowUptake}|} \tag{5}$$

II. $lowUptake_{error}$, a quantity metric assessing difference between the $DSC_{lowUptake}$ in eqn. (5) to the $DSC_{lowUptake}$ in the static PET_{sta} image, relative to the $DSC_{lowUptake}$ with equal tracer uptake in both high- and lowUptake sub-volumes for the matching segmentation method and target.

$$lowUptake_{error} = \frac{DSC_{lowUptake}^{sta,4D,mot,deb} - DSC_{lowUptake}^{sta}}{DSC_{lowUptake}^{sta}(uptakeRatio=4:4)} \tag{6}$$

An illustration of the volume similarity is provided in Figure 2. The lower and upper limits were ± 1. A lower limit of -1 for the instance of $DSC_{lowUptake}^{sta} = DSC_{lowUptake}^{sta}(uptakeRatio = 4:4:1)$ and no PET segmented fragment of the $CT_{lowUptake}$ sub-volume i.e., $DSC_{lowUptake}^{4D,mot,deb} = 0$. The upper limit of +1 while $DSC_{lowUptake}^{sta} = 0$ and the PET segmented amount of the $CT_{lowUptake}$ matches the homogeny uptakeRatio i.e., $DSC_{lowUptake}^{4D,mot,deb} = DSC_{lowUptake}^{sta}(uptakeRatio = 4:4:1)$.

By definition, $\Delta Vol = 0$ and the $lowUptake_{error} = 0$ for every instance of segmentation in the PET_{sta} scan protocol. The ΔVol and $lowUptake_{error}$ were compared to corresponding segmentations in the static PET_{sta} images for identically target volumes and uptakeRatios with a 5% significance level for a one-sample t-test.

Results

The $CT_{highUptake}$ and $CT_{lowUptake}$ volumes (mean ± 1 sd) deviations from the actual cavity volumes were 2 % ± 4 % for targets A and B, while the target C deviation was -5 % ± 5 %. The background measured SUV PET tracer activity (mean ± 1 sd) was 1.00 ± 0.06, including all FDG-PET tracer uptakeRatios. Summary tables of the ΔVol and $lowUptake_{error}$ metric are listed in Table 2 and Table 3, respectively. Apart from the Max40% segmentation method the PET_{4D} scans produced enlarged segmented volumes compared to the PET_{sta} scans with an increased ΔVol for the SUV40% of 2 % (p = 0.001), gradientSeg of 4 % (p = 0.03) and the 2.5SUV of 4 % (p < 0.001), including all six PET bins. The $lowUptake_{error}$ of the PET_{4D} was not significantly different from $lowUptake_{error}$ of the PET_{sta} for any segmentation method. For the PET_{mot} scan protocol, the ΔVol significantly increased for the Max40% of 15% (p < 0.001) and gradientSeg of 43 % (p < 0.001) methods compared to the PET_{sta} images. No significant changes in the ΔVol were observed for the SUV40% and 2.5SUV methods in the PET_{mot} scan protocol. A significant increase in the $lowUptake_{error}$ quantity of 0.33 was detected for the PET_{mot} scan protocol using the GradientSeg method (p < 0.001). None of the three methods Max40%, SUV40% or 2.5SUV provided $lowUptake_{error}$ in the PET_{mot} protocol significantly different

from the lowUptake$_{error}$ in the PET$_{sta}$ protocol. In the motion corrected PET$_{deb}$ scan protocol the Max40% (p < 0.001) and SUV40% (p = 0.03) methods both presented increased segmented volumes of 10 % and 6 % respectively, compared to the PET$_{sta}$ scan protocol. The 2.5SUV method presented a lower segmented volume of -4 % in PET$_{deb}$, in which marginally significant difference was found compared to the PET$_{sta}$ scan protocol (p = 0.048). In the PET$_{deb}$ scan the GradientSeg segmentations was not significantly different from the PET$_{sta}$ scan protocol according to both the ΔVol and lowUptake$_{error}$ quantity. As the only segmentation method the Max40% presented a lowUptake$_{error}$ metric that was significantly different in the PET$_{deb}$ scan protocol compared to the PET$_{sta}$ (p = 0.04).

Discussion

This study aimed to quantify PET segmentation methods according to static PET acquisitions combined with motion and an adjacently placed lowUptake volume interfered target lesions. The study design allocated the highUptake volume within every instance of segmentation. When motion was applied, the activity in the highUptake volume (as well as the lowUptake sub-volume) was partially displaced in the direction of the lowUptake location, simulating an overflow effect into the lowUptake location. For the instance of cone shaped volume (target C), the overflow effect would be from the cone wide-end highUptake sub-volume into the neighbouring lowUptake cone. This study design and the motion effect restricted to one dimension (superior-inferior) are limitations that may not be directly equivalent to the clinical conditions. This study categorized inconsistencies between widely used segmentation methods to evaluate the combined motion and target uptake heterogeneity combinations for different target to background FDG-tracer activity levels. Excluding the Max40% method, the segmented volumes in PET$_{4D}$ were slightly increased compared to the PET$_{sta}$ protocol. The residual motion in the PET bins connecting the inhale and exhale respiratory phases could explain the increasing volumes in PET$_{4D}$. However, the narrow confidence interval of the ΔVol in PET$_{4D}$ points to the scan protocol was consistent with segmentations in PET$_{sta}$. The lowUptake$_{error}$ quantities in PET$_{4D}$ supported segmentations consistent with the PET$_{sta}$ scan protocol as no significant deviation was detected. This finding was consistent to the result obtained by Bettinardi et al. (11); thus for these investigated segmentation methods, a six bin 4D-PET is recommended to be sufficient for motion-free image acquisition with an amplitude of 15 mm.

For the motion involved PET$_{mot}$ scan protocol the segmented volumes were enlarged, except for the 2.5SUV segmentation method. In both PET$_{mot}$ and PET$_{deb}$ the 2.5SUV method provided segmentations that were equivalent to the PET$_{sta}$ acquisition. In contrast to the other two threshold based segmentation methods (Max40% and SUV40%), the 2.5SUV method did not involve the maximum intensity, which degrades in motion-disturbed image acquisitions (21). Eroded SUV values may not necessarily correspond to different

volume of segmentations, as long as the SUV remains above the threshold value. Different constellations of the uptakeRatios are likely to affect the results in PET$_{mot}$ images in which the threshold values are close to the target SUV. The Max40% method exclusively relies on the maximum SUV, whereas the SUV40% method also facilitated background SUV correction. Due to the degraded SUV of PET$_{mot}$ images, a lower absolute threshold SUV value was used for Max40% segmentation compared to the SUV40%, thus segmenting slightly enlarged volumes relative to the SUV40%.

In particular, the GradientSeg method presented for both the segmented volume and the amount of lowUptake sub-volume, which were increased foremost in the PET$_{mot}$ protocol. Because the GradientSeg method makes use of intensity gradients as segmentation boundaries the enlarged volume, including the lowUptake sub-volume, was expected as a consequence of motion blur. This finding was supported by the PET$_{deb}$ scan protocol, which revealed that the segmentations were equivalent to PET$_{sta}$ scan protocol due to the motion correction with a re-establishment of the image intensity gradients.

Motion corrections through PET image deblurring with a position density estimate rely on accurate 4D-CT target detection. Due to the centre-off-masse uncertainties within 4D-CT phases, the position density K$_{motion}$ estimate may potentially result in an inaccurate processing of the deblurred PET image. For instance, an increased number of bins in 4D-CT may increase the temporal centre-of-mass detection and high contrast fiducials could clarify detection within each phases and limit uncertainties within K$_{motion}$ determination. Detecting fiducial centre-of-masses within a 4D-CT scan are still limited by other factors such as the velocity during CT phase bin acquisition, orientations and fiducial style (22). Furthermore, local deblurring must be performed near distinct lesions due to the various respiratory motion trajectories inside the lungs (23).

The main restrictions of the current study are the limited number of different tracer heterogeneity values and target geometries. In particular, heterogeneous PET lesions have been reported to be challenging to delineate for threshold based methods and thereby suggesting sophisticated methods instead (24). This current study exposed the similarity of the segmentation methods relative to a motionless PET acquisition. With segmentation evaluation relative to static PET segmentations, reliable ground-truth tumour volume description in static PET images is fundamental. The study by Wanet et al. revealed high accuracy for the GradientSeg method in 4D-PET compared to the surgical specimens of lung cancers (20). A closely related study by Yu et al. published an optimal SUV threshold close to 3.0 with a threshold of 2.5 SUV that was not significantly different from the surgical specimens (8). These related studies assessing the accuracies of PET segmentations according to pathological findings indicate a routine recommendation of the GradientSeg or 2.5 SUV segmentation. The findings in the present study identifying the discrepancies in PET segmentation, with and without motion-correction, combined with heterogeneous tracer uptake indicates that caution should be used with maximum intensities for threshold segmentation. In addition, severe overestimation

potentially exists for the GradientSeg method in non-corrected motion influenced PET images. For the instance of motion affected target lesions and the absence of 4D-PET or 3D-PET motion correction, the 2.5SUV segmentation method is recommended.

Conclusion

This experimental study of target lesions with heterogeneous tracer (FDG) uptake combined with respiratory motion demonstrated that motion-corrected PET imaging and the GradientSeg method provided the most consistent and accurate PET segmentation amongst the tested segmentation methods.

Conflicts of interest

None to declare. The authors alone are responsible for the content and writing of the paper.

Acknowledgements

Tables:

Table 1: SUV threshold values.

uptakeRatio	4:4:1	3:2:1	4:2:1	8:3:1
Max40%	*1.6*	*1.2*	*1.6*	**3.2**
SUV40%	*2.2*	*1.8*	**2.2**	**3.8**
GradientSeg	*NA*	*NA*	**NA**	**NA**
2.5 SUV	*2.5*	**2.5**	**2.5**	*2.5*

SUV threshold values among the tracer uptakeRatios and segmentation methods. Grey cells indicate the predicted segmentation of the highUptake volume only, whereas white cells indicate predicted segmentation of both the high- and lowUptake volumes. The non-threshold method GradientSeg was marked not available (NA). The GradientSeg low/high-Uptake separation were predicted assuming accurate PET_{static} segmentation.

Table 2: ΔVol of the PET segmentations.

Method	PET_{4D}	PET_{mot}	PET_{deb}
Max40%	0.01 [-0.01; 0.03]	0.15 [0.11; 0.19]	0.10 [0.06; 0.14]
SUV40%	0.02 [0.01; 0.03]	0.06 [0.00; 0.12]	0.06 [0.01; 0.12]
GradientSeg	0.04 [0.00; 0.07]	0.43 [0.12; 0.74]	0.04 [-0.11; 0.20]
2.5 SUV	0.04 [0.02; 0.05]	-0.04 [-0.11; 0.02]	-0.04 [-0.08; 0.00]

Mean with 95% CI volume differences (relative to PET_{sta}) of the 4D, motion and deblurred PET protocols separated into segmentation methods, including all tracer uptakeRatios and target volumes.

Table 3: The $lowUptake_{error}$ metric of the PET segmentations.

Method	PET_{4D}	PET_{mot}	PET_{deb}
Max40%	0.00 [-0.05; 0.04]	0.09 [-0.02; 0.20]	0.10 [0.00; 0.20]
SUV40%	0.04 [-0.01; 0.08]	0.12 [0.00; 0.24]	0.13 [-0.01; 0.28]
GradientSeg	0.01 [-0.03; 0.06]	0.33 [0.08; 0.58]	0.08 [-0.04; 0.21]
2.5 SUV	0.00 [-0.03; 0.04]	0.03 [-0.06; 0.13]	0.07 [-0.03; 0.17]

Mean with 95% CI of the $lowUptake_{error}$ of the 4D, motion and deblurred PET protocols separated between segmentation methods, including all tracer uptakeRatios and target volumes.

Internal diameter = 39 mm

Internal diameter 0.4 - 26 mm

60 mm

A2

A1

30 mm

70 mm

B2

B1

35 mm

C1

C2

30º

Length 30 mm

Internal separation = 3.4 mm

Vol. A1 = 31.5 cm^3

Vol. A2 = 21.8 cm^3

Vol. B1 = 31.5 cm^3

Vol. B2 = 29.5 cm^3

Vol. C1 = 9.7 cm^3

Vol. C2 = 9.7 cm^3
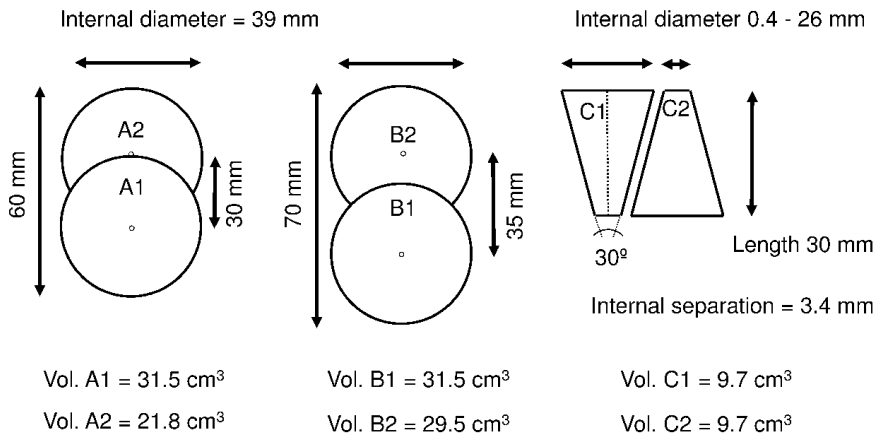
Figure 1: Target volumes (A, B and C) with the actual internal volume size [cm^3]. The Target high sub-volumes are denoted by one (A1, B1 & C1) and the Target low sub-volume as two (A2, B2 & C2). Targets A and B consisted of interlaced spheres, whereas the target C involved two cones aligned side-by-side in opposing direction.
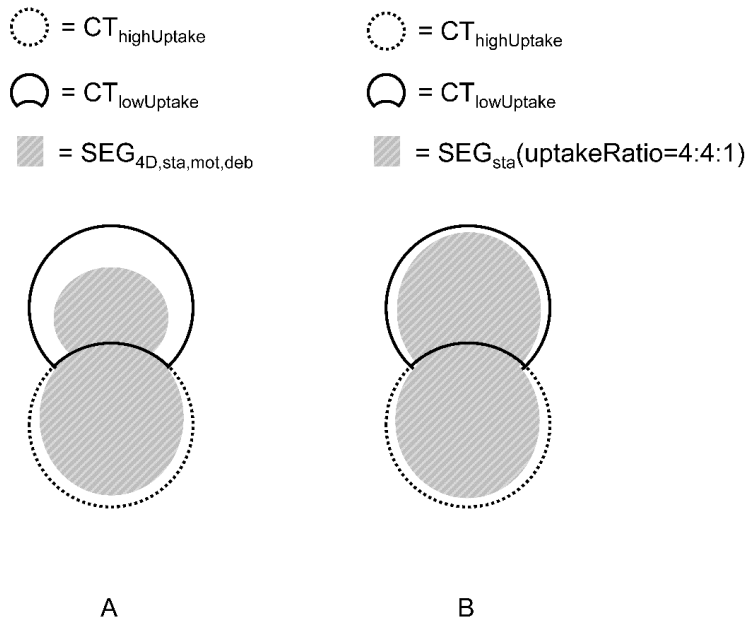
Figure 2: Relationship between the PET segmented volume SEG$_{4D,sta,mot,deb}$ and the lowUptake reference volume CT$_{lowUptake}$ used to define the lowUptake$_{error}$ quantity. Sub-figure A illustrates a situation where the lowUptake sub-volume was partially segmented and in sub-figure B, a homogeneous tracer uptakeRatio = 4:4:1 illustrated optimal lowUptake segmentation.

Reference List

(1) Editor: Hansen O. DOLG's Radioterapigruppens Rekommendationer for udførelse af strålebehandling ved lungekræft. Available from: http://www.dolg.dk.

(2) Engholm G, Ferlay J, Christensen N, Bray F, Gjerstorff ML, Klint A, et al. NORDCAN: Cancer Incidence, Martality, Prevalence and Survival in the Nordic Contries, Version 7.1 (09.07.2015). Association of the Nordic Cancer Registries. Danish Cancer Society. Available from http://www.ancr.nu, accessed on day/month/year.

(3) Goldstraw P, Editor. Staging Manual in Thoracic Oncology. International Association For The Study of Lung Cancer, 2009.

(4) Heusch P, Buchbender C, Kohler J, Nensa F, Gauler T, Gomez B, et al. Thoracic staging in lung cancer: prospective comparison of 18F-FDG PET/MR imaging and 18F-FDG PET/CT. J Nucl Med 2014 Mar;55(3):373-8.

(5) Konert T, Vogel W, MacManus MP, Nestle U, Belderbos J, Gregoire V, et al. PET/CT imaging for target volume delineation in curative intent radiotherapy of non-small cell lung cancer: IAEA consensus report 2014. Radiother Oncol 2015 Jul;116(1):27-34.

(6) Edet-Sanson A, Dubray B, Doyeux K, Back A, Hapdey S, Modzelewski R, et al. Serial assessment of FDG-PET FDG uptake and functional volume during radiotherapy (RT) in patients with non-small cell lung cancer (NSCLC). Radiother Oncol 2012 Feb;102(2):251-7.

(7) Werner-Wasik M, Nelson AD, Choi W, Arai Y, Faulhaber PF, Kang P, et al. What is the best way to contour lung tumors on PET scans? Multiobserver validation of a gradient-based method using a NSCLC digital PET phantom. Int J Radiat Oncol Biol Phys 2012 Mar 1;82(3):1164-71.

(8) Yu J, Li X, Xing L, Mu D, Fu Z, Sun X, et al. Comparison of tumor volumes as determined by pathologic examination and FDG-PET/CT images of non-small-cell lung cancer: a pilot study. Int J Radiat Oncol Biol Phys 2009 Dec 1;75(5):1468-74.

(9) Steenbakkers RJ, Duppen JC, Fitton I, Deurloo KE, Zijp LJ, Comans EF, et al. Reduction of observer variation using matched CT-PET for lung cancer delineation: a three-dimensional analysis. Int J Radiat Oncol Biol Phys 2006 Feb 1;64(2):435-48.

(10) Calais J, Thureau S, Dubray B, Modzelewski R, Thiberville L, Gardin I, et al. Areas of high 18F-FDG uptake on preradiotherapy PET/CT identify preferential sites of local relapse after chemoradiotherapy for non-small cell lung cancer. J Nucl Med 2015 Feb;56(2):196-203.

(11) Bettinardi V, Rapisarda E, Gilardi MC. Number of partitions (gates) needed to obtain motion-free images in a respiratory gated 4D-PET/CT study as a function of the lesion size and motion displacement. Med Phys 2009 Dec;36(12):5547-58.

(12) Foster B, Bagci U, Mansoor A, Xu Z, Mollura DJ. A review on segmentation of positron emission tomography images. Comput Biol Med 2014 Jul;50:76-96.

(13) Greco C, Rosenzweig K, Cascini GL, Tamburrini O. Current status of PET/CT for tumour volume definition in radiotherapy treatment planning for non-small cell lung cancer (NSCLC). Lung Cancer 2007 Aug;57(2):125-34.

(14) Aristophanous M, Penney BC, Martel MK, Pelizzari CA. A Gaussian mixture model for definition of lung tumor volumes in positron emission tomography. Med Phys 2007 Nov;34(11):4223-35.

(15) Geets X, Lee JA, Bol A, Lonneux M, Gregoire V. A gradient-based method for segmenting FDG-PET images: methodology and validation. Eur J Nucl Med Mol Imaging 2007 Sep;34(9):1427-38.

(16) Biehl KJ, Kong FM, Dehdashti F, Jin JY, Mutic S, El N, I, et al. 18F-FDG PET definition of gross tumor volume for radiotherapy of non-small cell lung cancer: is a single standardized uptake value threshold approach appropriate? J Nucl Med 2006 Nov;47(11):1808-12.

(17) Le MA, Hatt M, Pradier O, Cheze-Le RC, Visvikis D. Impact of the accuracy of automatic tumour functional volume delineation on radiotherapy treatment planning. Phys Med Biol 2012 Sep 7;57(17):5381-97.

(18) Park SJ, Ionascu D, Killoran J, Mamede M, Gerbaudo VH, Chin L, et al. Evaluation of the combined effects of target size, respiratory motion and background activity on 3D and 4D PET/CT images. Phys Med Biol 2008 Jul 7;53(13):3661-79.

(19) El N, I, Low DA, Bradley JD, Vicic M, Deasy JO. Deblurring of breathing motion artifacts in thoracic PET images by deconvolution methods. Med Phys 2006 Oct;33(10):3587-600.

(20) Wanet M, Lee JA, Weynand B, De BM, Poncelet A, Lacroix V, et al. Gradient-based delineation of the primary GTV on FDG-PET in non-small cell lung cancer: a comparison with threshold-based approaches, CT and surgical specimens. Radiother Oncol 2011 Jan;98(1):117-25.

(21) Park SJ, Ionascu D, Killoran J, Mamede M, Gerbaudo VH, Chin L, et al. Evaluation of the combined effects of target size, respiratory motion and background activity on 3D and 4D PET/CT images. Phys Med Biol 2008 Jul 7;53(13):3661-79.

(22) Nielsen MS, Nystrom MW, Carl J. Potential position errors using fiducial markers for gated image guided radiotherapy. Acta Oncol 2013 Oct;52(7):1472-6.

(23) Seppenwoolde Y, Shirato H, Kitamura K, Shimizu S, van HM, Lebesque JV, et al. Precise and real-time measurement of 3D tumor motion in lung due to breathing and heartbeat, measured during radiotherapy. Int J Radiat Oncol Biol Phys 2002 Jul 15;53(4):822-34.

(24) Hatt M, Cheze-Le RC, van BA, Lambin P, Pradier O, Visvikis D. Impact of tumor size and tracer uptake heterogeneity in (18)F-FDG PET and CT non-small cell lung cancer tumor delineation. J Nucl Med 2011 Nov;52(11):1690-7.

Paper III

A new method to validate thoracic CT-CT deformable image registration using auto-segmented 3D anatomical landmarks

Nielsen MS, Østergaard LR, Carl J

The study aimed to develop a new method to validate thoracic CT co-registrations through anatomical landmarks extracted from bronchial airway segmentation. Five previously diagnosed lymphoma patients were CT scanned three times. The latter two CT scans were registered to the initial CT scan using Demons, B-spline and Affine image registration algorithms. The bronchial airways were segmented using automatic wavefront segmentation from a seed point within the upper trachea. The bronchial branch point positions were identified and matched against corresponding bronchial branch points for the registered images. The image registrations were validated using Dice similarity coefficient (DSC) for the body volumes, the lungs and deviations between corresponding bronchial branch points. The bronchial branch point deviations and the DSC of both the body and the lungs presented the highest registration accuracy with the B-spline algorithm followed by the Demons and finally the Affine algorithm. The B-spline and Demons algorithms both presented local branch point deviations close to 15 mm. In conclusion, the bronchial branch point demonstrated validation of image registration with identification of local misalignment within the lung region.

ORIGINAL ARTICLE

A new method to validate thoracic CT-CT deformable image registration using auto-segmented 3D anatomical landmarks

MARTIN S. NIELSEN[1], LASSE R. ØSTERGAARD[2] & JESPER CARL[1]

[1]*Department of Medical Physics, Aalborg University Hospital, Denmark and* [2]*Department of Health Science and Technology, Aalborg University, Denmark*

ABSTRACT

Background. Deformable image registrations are prone to errors in aligning reliable anatomically features. Consequently, identification of registration inaccuracies is important. Particularly thoracic three-dimensional (3D) computed tomography (CT)-CT image registration is challenging due to lack of contrast in lung tissue. This study aims for validation of thoracic CT-CT image registration using auto-segmented anatomically landmarks.
Material and methods. Five lymphoma patients were CT scanned three times within a period of 18 months, with the initial CT defined as the reference scan. For each patient the two successive CT scans were registered to the reference CT using three different image registration algorithms (Demons, B-spline and Affine). The image registrations were evaluated using auto-segmented anatomical landmarks (bronchial branch points) and Dice Similarity Coefficients (DSC). Deviation of corresponding bronchial landmarks were used to quantify inaccuracies in respect of both misalignment and geometric location within lungs.
Results. The median bronchial branch point deviations were 1.6, 1.1 and 4.2 (mm) for the three tested algorithms (Demons, B-spline and Affine). The maximum deviations (> 15 mm) were found within both Demons and B-spline image registrations. In the upper part of the lungs the median deviation of 1.7 (mm) was significantly different ($p < 0.02$) relative to the median deviations of 2.0 (mm), found in the middle and lower parts of the lungs. The DSC revealed similar registration discrepancies among the three tested algorithms, with DSC values of 0.96, 0.97 and 0.91, for respectively Demons, B-spline and the Affine algorithms.
Conclusion. Bronchial branch points were found useful to validate thoracic CT-CT image registration. Bronchial branch points identified local registration errors > 15 mm in both Demons and B-spline deformable algorithms.

The number of different medical imaging modalities has been increasing steadily since the early introduction of computed tomography (CT). In recent years positron emission tomography (PET) and magnetic resonance imaging (MRI) scanners are becoming clinical standard in oncology [1]. Consequently, multiple modalities of different three-dimensional (3D) medical image examinations are used. In order to fuse information from multiple modality images or to correlate information between single modality images, image registration are required. As an example, single modality intra-subject image registration is becoming essential in radiotherapy to detect pulmonary changes [2,3].

In general, the concept of image registration is a way to create a spatial transformation from one image into another image based on voxels properties or image features [4,5]. For registration of medical images non-rigid approaches defined as deformable image registration (DIR) [6,7] are increasingly becoming the preferable registration procedure. The DIR algorithms can be categorized as parametric and non-parametric models [5]. A parametric model, such as the B-spline, interpolates the transformation with spline models using a grid of control points [8]. A widely used non-parametric model is the Demons method [4,9]. The Demons method is an intensity-based algorithm, which uses local gradients on the static reference image to derive a displacement vector field as a transformation of the registered image. Another non-rigid method with semi-elastic properties is the Affine transformation. The Affine

Correspondence: M. S. Nielsen, Department of Medical Physics, Aalborg University Hospital, Denmark. Tel: + 45 97661591. E-mail: martin.skovmos.nielsen@rn.dk

image registration use the rigid linear transformation combined with isotropic scaling and shearing transformations [8].

Potentially, the DIR algorithms may produce unrealistic deformations and consequently validation of registration accuracies is important. Previous studies designed for evaluation of DIR methods and algorithms have provided different methods for validation. Typically, grayscale differences, volume coincident or identifiable anatomical landmarks have been used to quantify image similarities. A validation method based on anatomical structure (landmark) appears to be a better choice for detection of unrealistic deformations [10,11]. Manual correlation of landmarks may be a time consuming process with potential interobserver variance. Consequently, an automatically process for landmark identification could benefit validation in image registration.

The aim of the present study was to validate anatomical landmarks for 3D image co-registration of thoracic CT-CT scans. The validation method was based on semi-automatically defined thoracic landmarks, defined as bronchial branch points, extracted from a segmented airway bronchial tree.

Material and methods

Five lymphoma patients were CT scanned three times within a period of 18 months (Supplementary Table I available online at http://informahealthcare.com/doi/abs/10.3109/0284186X.2015.1061215). All patients followed a protocol with a low dose full body CT scan in combination with a PET scan, as a follow-up after primary treatment (chemotherapy). The patients were scanned in supine position with the arms above the head. The CT scanner settings were 120 kVp, 35–90 mA, reconstructed with a slice thickness of 0.625 mm. The CT slices selected for image registration were from the first thoracic vertebra and 400 CT slices below covering 25 cm of the thorax including the total lung volume. For each patient the initial CT scan was defined as the reference scan (fixed CT). The two subsequent CT scans were co-registered to the reference CT volume using three different non-rigid methods: Demons, B-spline and Affine. Succeeding image registration the bronchial airways were segmented and bronchial branch point identified.

Landmark definition

A seed point in trachea, defined as the lowest CT density value inside the body volume of the first CT slice, initialized a wavefront propagation described by Stephansen et al. [12] and incorporated as MAT-LAB functions. The wavefront propagation expanded

the airway segmentation through multiple bronchial branch points using an initial adaptive grayscale threshold of -750 HU. A series of wavefronts propagated until reaching the HU threshold or a bronchial branch point. By increasing the threshold iteratively additional voxels were included within the wavefront. The wavefront expanded until leakage detection occurred, either by excessing a wavefront expansion factor or a segment expansion factor. A wavefront expansion factor of 2.8 and a segment expansion factor of 1.5 similar to the proposed values by Stephansen et al. [12] were used. A skeleton, defined as the centroid of the airway segment within each CT slice, was extracted with information of both parental segments and possible children segments. The skeleton information was used for bronchial branch point definition. A bronchial branch point was defined as the final skeleton coordinate (x,y,z), in the presence of at least two children segments. Coordinates of the bronchial branch points were automatically assigned relative to the origin of each of the CT volumes. 3D Euclidean distance deviations between equivalent bronchial branch points formed a metric of residuals following image registration. Corresponding bronchial branch points were identified manually by following the skeleton through equivalent branches. Only corresponding branch points, with identical number of child segments, were selected for evaluation of branch point deviations. Coordinates of the bronchial branch points were categorized into three superior-inferior positions within the lungs: upper, middle and lower positions, as demonstrated in Figure 1A.

Volume similarity

Image similarities using Dice Similarity Coefficient (DSC) [13] were defined for the overall patient volume (body) and a sub volume of the body covering the airways (lungs). The body volume was defined by creating a binary image, covering voxels above -200 HU, and post-processing to fill low-density cavities. Through indexing of the 3D binary image, into objects according to enclosed number of voxels, non-patient support equipment was removed by keeping the largest object (patient body). The lungs were defined as the sub volume of voxels within an upper threshold of -700 HU and connected to the trachea. Finally, a post-processing procedure filling detached cavities (lung parenchyma) within the lung volume, associated airway intensity values above -700 HU to the lung volume.

Registration methods

The Demons algorithm was a commercial available algorithm, Varian Medical Systems Smart Adapt Ver.

(A)   **(B)**

Reference image
Registered image

Right upper   Left upper

Right middle   Left middle
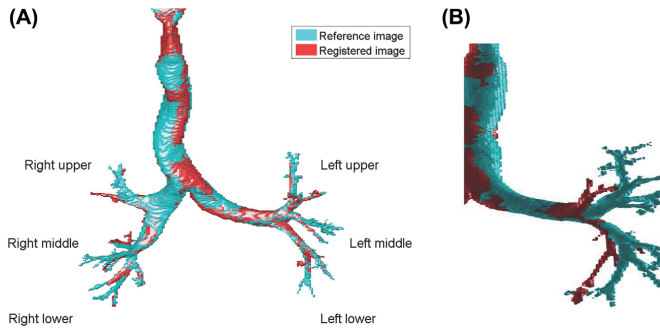
Right lower   Left lower

Figure 1. (A) Airway segmentation for a reference image (blue) with overlay of a registered image (red). Three superior-inferior positions for the bronchial bifurcations were defined as: upper, middle and lower lung positions. The bronchial branch point in the upper right and left lung segment were classified to the upper position. The right middle lung- and the ligulae segment in the left lung were classified as middle position and the right and left lower lung segment were classified to the lower position. (B) Bronchial segment following image registration where local deformations result in misaligned airway segment.

11.0, described by Thirion et al. [9]. The B-spline and Affine algorithms consisted of MATLAB functions, incorporated in procedures developed for this study. The Demons image registration features the options of both rigid and deformable registration, which allowed a rigid registration prior to the deformable registration. The volume of interest for the rigid image registrations was primary the CT scanner couch. The following volume of interest, for the deformable registration, contained the entire thoracic volume including the patient surface but excluding the scanner couch. The two MATLAB established methods, B-spline and Affine image registrations, used a rigid CT-CT procedure, prior to the final registration. The rigid registration synchronized the CT scans according to couch position, origin and reconstruction diameter. The B-spline image registration algorithm consisted of MATLAB optimization functions from Mathworks File Exchange [14]. The B-spline image registration optimization used an initial uniform grid of control points with an isotropic internal spacing corresponding to 30 mm (x,y,z). The optimizer used a Limited-memory Broyden-Fletcher-Goldfarb-Shanno (L-BFGS) with a maximum number of 50 iterations and a squared sum difference for image similarity metric. The Affine image registrations used a 3D image registration procedure with the 'Image Processing Toolbox' for MATLAB 2013b. This algorithm used a regular step gradient descent for optimization with 100 iterations and default settings except for the initial step in the optimizer, which was set at 0.15 (named MaximumStep-Length in MATLAB Image Processing Toolbox). As an image similarity metric a mean squared difference of voxel intensities were used.

Statistical analysis

Corresponding bronchial branch point were analyzed using a multi-way ANOVA comparison test adjusting for variations within algorithms, patients and superior-inferior position inside the lungs. Deviations are expressed as median (mm) with 95% confidence interval (95% CI). The DSC, expressed with 95% CI, were analyzed using a multi-way ANOVA comparison test adjusting for variations within algorithms, volumes (body and lungs) and patients. Significant differences were considered for p-values less than 0.05.

Results

A total number $N = 738$ corresponding set of bronchial branch points were identified (ranging from 43 to 103 in individual patients). The airway segmentation process defined the bronchial tree up to 15 cm from the main trachea bifurcation. The 3D reproducibility in branch point position were 0.6 mm (upper lung), 0.1 mm (middle lung) and 0.2 mm (lower lung). The reproducibility, defined by one standard deviation of bronchial branch points, originated from a single test CT by forcing the algorithm to segment from an initial threshold values in the range -650 to -800 HU (similar to the range used by the iterations). Table I contains a summary of bronchial branch point deviation divided into groups of patients, algorithms and superior/inferior position inside lungs. For patients the median deviation ranged from 1.4 to 2.5 mm and were significantly different between patients ($p < 0.01$). The tested algorithms differed significantly ($p < 0.01$). Median

Table I. The median bronchial branch point deviations following image registration.

Variable	Median (mm)	95% CI (mm)
Patient		
1	1.4	(1.2; 1.5)
2	2.2	(1.9; 2.5)
3	1.8	(1.6; 2.0)
4	2.5	(2.2; 2.8)
5	2.0	(1.7; 2.3)
Algorithm		
Demons	1.6	(1.4; 1.7)
B-spline	1.1	(1.0; 1.2)
Affine	4.2	(3.8; 4.7)
Branch position		
Upper lung	1.7	(1.6; 1.9)
Middle lung	2.1	(1.9; 2.3)
Lower lung	2.0	(1.8; 2.2)

deviations ranged from 1.1 mm (B-spline), 1.6 mm (Demons) to 4.2 mm (Affine). A significant lower deviation of bronchial branch point ($p = 0.02$) was observed in the superior part of the lung, compared to the middle/lower lung part. The median deviations were 1.7 mm, 2.1 mm and 2.0 mm in the upper, middle and lower part of the lungs, respectively. No significant difference was found between the middle and lower sited bronchial branches. A quantile distribution of the branch point deviations (Table II), grouped by algorithms and superior-inferior positions distinguish the two locally deformable algorithms (Demons and B-spline) medians from the Affine. For the locally deformable algorithms, 95% of the bronchial branch points were registered within 5 mm. For the Affine algorithm, 95% of the branch points were registered within 10 mm. The observed maximum bronchial deviations were for the Demons 16 mm (middle lung), B-spline 15 mm (upper lung) and Affine 13 mm (upper and middle). Figure 1B

Table II. Centile distribution of the bronchial branch point deviation in (mm).

	Centile	5%	25%	50%	75%	95%	Max deviation
Demons	Combined	1	1	2	2	5	16
n = 108	Upper	1	1	2	2	4	7
n = 60	Middle	1	1	2	2	12	16
n = 71	Lower	1	1	2	2	3	6
B-spline	Combined	0	1	1	2	5	15
n = 105	Upper	0	1	1	2	3	15
n = 80	Middle	0	1	1	2	6	10
n = 86	Lower	0	1	1	2	8	9
Affine	Combined	1	3	5	6	10	13
n = 102	Upper	2	3	4	5	10	13
n = 56	Middle	1	3	4	6	10	13
n = 70	Lower	1	4	5	6	9	12

Bronchial branch point deviations (total n = 738) for all five patients divided into the three algorithms and superior/inferior position inside the lungs.

Table III. The body and lung DSC following image registration.

Dice coefficients	Body volume 95% CI	Lung volume 95% CI
Demons	0.99 (0.98; 0.99)	0.96 (0.96; 0.96)
B-spline	0.99 (0.99; 0.99)	0.97 (0.97; 0.98)
Affine	0.96 (0.96; 0.97)	0.91 (0.88; 0.95)

DSC calculated for all patients and scans separated into two volumes and the three algorithms.

demonstrates a local deformation with consequently misaligned airway structures.

The image registrations produced a higher DSC for the body, compared to the lung volume ($p < 0.01$). Additionally, significant different DSCs were found between the algorithms ($p < 0.01$) (Table III). The B-spline image registrations yield the maximum DSC, whereas the Affine transformation produced the lowest accuracy according to the DSC. No significant differences of the DSCs among the five patients were found. The mean lung surface differences, using Euclidian distance metric with 95% CI, were for the Demons algorithm 2.2 mm (2.1; 2.2) mm, B-spline 2.1 mm (2.0; 2.2) mm and the Affine 3.1 mm (2.5; 3.7) mm.

Discussion

The present study aimed to evaluate different DIR methods, based on automatically segmented bronchial branch points using corresponding anatomical landmarks. Despite the automatically process of detecting bronchial branch points, identification of corresponding branch points revealed a time consuming task. Primary due to classification of superior/inferior position and the different number of sub-bronchial segmentations, as illustrated in Figure 1. The image material for this study consisted of low dose CT scans, which influenced on the image quality compared to a normal CT. The low dose CT may limit the bronchial tree segmentation in each lung volume. Normal dose or even better high resolution diagnostic CT would most likely give an enhanced segmentation of the bronchial tree. Excluding the most distant parts of the bronchial tree would most likely eliminate the tedious manual task of checking for corresponding landmarks.

The present study revealed discrepancies of image registrations between the three tested algorithms. Despite a good median accuracy for image registration with local deformations (Demons and B-spline), the maximum branch point deviations showed a potential risk of large local deformation errors of approximately 15 mm. These maximum bronchial branch deviations appeared in the middle lung for the Demons algorithm and in the upper lung for the

B-spline algorithm. Particularly the bronchial branches in the upper lung demonstrated the lowest median deviation of 1.7 mm, but for the B-spline algorithm a misalignment of 15 mm as well. Identification of such a registration error would be crucial for high dose thoracic radiotherapy with the bronchi as an organ at risk [15]. The bronchial branch point deviations for the Affine method was expected to be higher relative to the deformable algorithms due the lack of ability local deformations within the image set. A study by Senthi et al. [16], comparing a rigid and deformable algorithm defined as contour differences, demonstrated improved registration accuracy by 3 mm when using the deformable registrations. In the present study a similar improvement of the median bronchial branch points were observed between the Affine and B-spline algorithm. Regarding the Demons and B-spline algorithms, both the DSC and the deviation between the bronchial branch points maintained a lower deviation for the B-spline. A general lower bronchial branch deviation for a B-spline algorithm was in agreement with a study by Varadhan et al. [5], which specified increased accuracy for the B-spline method compared to a Demons algorithm. The work from Varadhan et al. dedicated a smoother deformations field for the B-spline method relative to a Demons algorithm as a reason for a more reliable deformation.

Landmarks as the bronchial branch point in the present study provided a reasonable method to validate image registrations comparable to the DSC. Using the DSC as a metric for image registration accuracy provided a significant higher image similarity for the body volume relative to the lungs. However, this might be related to the mathematical definition of the DSC, consequently the DSC may not be appropriate for large volume associations. The DSC confirmed significant differences among all three tested image registration algorithms, in the favor of the B-spline algorithm. In contrast to the DSC quantity landmark identifications provided additional information related to local misaligned image registrations.

A main limitation, using the bronchial tree as landmark identifications, is the ability to segment the airway tree and thus define the bronchial branch points. This could be of concern for patients with partial airway obstruction or severe lung density changes due to radiotherapy [3,17]. Chow et al. specified the requirement for DIR for proper detection and follow-up of lung injury succeeding chemoradiotherapy. For images decomposed by density changes, the segmented airways as well as a map of corresponding bronchial branch point have prospect for usage within DIRs. A study by Vasquez Osorio et al. [18] revealed CT-MR image registration, established

on automatic vessel segmentation of the liver in the two image modalities. Their method has the potential for adaption in thoracic CT-CT co-registration, where local deformation within the lung volume could be improved using segmented airways.

In conclusion, the present study demonstrated a lower median overall registration error when using the B-spline algorithm compared to the Demons and Affine algorithm. However, local registrations errors of approximately 15 mm were identified for both the Demons and B-spline algorithms using the bronchial branch points for validation of image registration.

References

[1] Partovi S, Kohan A, Rubbert C, Vercher-Conejero JL, Gaeta C, Yuh R, et al. Clinical oncologic applications of PET/MRI: A new horizon. Am J Nucl Med Mol Imaging 2014;4:202–12.

[2] Cella L, Liuzzi R, D'Avino V, Conson M, Di Biase A, Picardi M, et al. Pulmonary damage in Hodgkin's lymphoma patients treated with sequential chemo-radiotherapy: Predictors of radiation-induced lung injury. Acta Oncol 2014;53:613–9.

[3] De Ruysscher D, Sharifi H, Defraene G, Kerns SL, Christiaens M, De Ruyck K, et al. Quantification of radiation-induced lung damage with CT scans: The possible benefit for radiogenomics. Acta Oncol 2013;52:1405–10.

[4] Sotiras A, Davatzikos C, Paragios N. Deformable medical image registration: A survey. IEEE Trans Med Imaging 2013;32:1153–90.

[5] Varadhan R, Karangelis G, Krishnan K, Hui S. A framework for deformable image registration validation in radiotherapy clinical applications. J Appl Clin Med Phys 2013;14:4066.

[6] Holden M. A review of geometric transformations for non-rigid body registration. IEEE Trans Med Imaging 2008;27:111–28.

[7] Kirby N, Chuang C, Ueda U, Pouliot J. The need for application-based adaptation of deformable image registration. Med Phys 2013;40:011702–10.

[8] Oliveira FP, Tavares JM. Medical image registration: A review. Comput Methods Biomech Biomed Engin 2014;17:73–93.

[9] Thirion JP. Image matching as a diffusion process: An analogy with Maxwell's demons. Med Image Anal 1998;2:243–60.

[10] Kadoya N, Fujita Y, Katsuta Y, Dobashi S, Takeda K, Kishi K, et al. Evaluation of various deformable image registration algorithms for thoracic images. J Radiat Res 2014;55:175–82.

[11] Murphy K, van Ginneken B, Reinhardt JM, Kabus S, Ding K, Deng X, et al. Evaluation of registration methods on thoracic CT: The EMPIRE10 challenge. IEEE Trans Med Imaging 2011;30:1901–20.

6   *M. S. Nielsen et al.*

[12] Stephansen UL, Horup RW, Olesen JT, Carl J, Korsager AS, Østergaard LR. Airway tree segmentation for optimal stent placement in image-guided radiotherapy: The fourth International Workshop on Pulmonary Image Analysis; 2011 Sep 18; Toronto, Canada. 2011 p. 135–46.

[13] Dice LR. Measures of the amount of ecologic association between species. Ecology 1945;26:297–302.

[14] Kroon DJ, editor. B-spline grid, image and point based registration [Internet]. File Exchange MATLAB Central, 2008. [Updated 2011 Mar 16]. Available from: http://www.mathworks.com/matlabcentral/fileexchange/20057-b-spline-grid--image-and-point-based-registration. [cited May 13 2015]

[15] Nielsen TB, Hansen O, Schytte T, Brink C. Inhomogeneous dose escalation increases expected local control for NSCLC patients with lymph node involvement without increased mean lung dose. Acta Oncol 2014;53:119–25.

[16] Senthi S, Griffioen GH, van Sornsen de Koste JR, Slotman BJ, Senan S. Comparing rigid and deformable dose registration for high dose thoracic re-irradiation. Radiother Oncol 2013;106:323–6.

[17] Chow TL, Louie AV, Palma DA, D'Souza DP, Perera F, Rodrigues GB, et al. Radiation-induced lung injury after concurrent neoadjuvant chemoradiotherapy for locally advanced breast cancer. Acta Oncol 2014;53:697–701.

[18] Vasquez Osorio EM, Hoogeman MS, Mendez RA, Wielopolski P, Zolnay A, Heijmen BJ. Accurate CT-MR vessel-guided nonrigid registration of largely deformed livers. Med Phys 2012;39:2463–77.

Supplementary material available online

Supplementary Table I available online at http://informahealthcare.com/doi/abs/10.3109/0284186X.2015.1061215.

CHAPTER 7. DISCUSSION

The thesis contributes to the field of radiotherapy primarily in relation to the systematic uncertainties in treatment preparation. The uncertainties described in the previous chapters focused on CT imaging fiducial detection and image guidance, PET imaging target segmentation with heterogeneous tracer uptake and motion distortions and validation of thoracic CT-CT image registration using extracted anatomical landmarks.

The fiducial detection methods in study I considered the centre-of-mass detection in 4D-CT and either centre-of-mass or end-points detections within image-guided X-ray verifications. The 4D-CT scans in this study assessed two slice thicknesses of 1.25 mm and 2.50 mm, which are comparable to clinical CT scans of patients. The study showed no differences between a slice thickness of 1.25 mm and 2.50 mm. This was unexpected, as the increased resolution with a slice thickness of 1.25 mm most likely improves fiducial centre-of-mass accuracy. Particularly for small fiducials located within a few CT slices, a CT slice thickness of 1.25 mm was expected to increase detection accuracy. Previous studies have assessed higher detection accuracies for small thoracic nodules with a decrease in CT slice thickness (80;81). The image-guided verification images using the BrainLAB Gated ExacTrac system assessed a mean offset of 0.15 mm with a standard deviation of approximately 0.6 mm. These outcomes were not affected by CT slice thickness, fiducial type or orientation and were close to the findings by Matney et al. (82). However, image acquisitions rely on tracking the external IR detectable spheres. Thus, a periodic regular motion trajectory provided the optimal conditions for image guidance using X-ray verifications in combination with respiratory correlated IR tracking. The offset and standard deviation should consequently imitate the minimum setup uncertainty within clinical margin considerations. The accuracy associated with fiducial speed within phase bin acquisition was in agreement with a study by Matney et. al (82). The new findings described in study I provided additional quantification of the uncertainties related to fiducial type and orientation within 4D-CT detection. The reduced detection accuracy for the 5mm NiTi stent could have clinical consequences for radiotherapy using a CT phase for treatment planning acquired for the duration of a high fiducial speed. For CT images acquired with low fiducial speed no significant detection differences were observed between fiducial type and orientation. For respiratory-gated radiotherapy in the inhalation or exhalation CT phases, the minimal fiducial speed during image acquisition resulted in the lowest standard deviation for fiducial detection. The systematic uncertainties defined by one standard deviation with fiducials in 4D-CT based radiotherapy ranged from 0.15 mm up to 2.50 mm for treatment planning in the mid-position or mid-ventilation CT phases. In particular, the mid-ventilation phase is commonly

used for treatment planning for non-gated radiotherapy (46;65;83). The uncertainties in study I must be considered to be conservative estimates, as irregular motions were ignored. Breathing patterns are likely to change from one cycle to another, from baseline drift and from session to session (25). For clinical considerations, multiple fiducials placed close to each target lesion would be optimal. A major issue with fiducials as target surrogates arises from positioning the fiducial near target sites. Different respiratory trajectories have been reported for different locations in the lungs, and repeated 4D-CT scans may provide various trajectories for the individual fiducials (71;84). The variation in respiratory trajectories throughout the lungs could impact the motion-compensated 3D-PET scan, described in Paper II. Uncertainty in motion trajectory would lead to uncertainty in definition of the position density estimate and in the deblurred PET image as well. The study design described in paper I and II using rigid 1D phantom motion may not correspond to clinical conditions. The simulation of respiratory motions was set to a rigid repeated motion cycle to limit variations between comparable measurements. In contrast, for actual patients, fluctuations within the respiratory cycle and amplitude as well as motion path changes between treatment preparation and radiotherapy could lead to variation in detection accuracies (71;85). However, for assessment of fiducial detections in CT and X-ray images, uncertainties related to inconsistent respiration cycles were discarded using this phantom setup. In study II, potential fluctuations of the motion may not affect PET segmentation in the same manner as X-ray acquisition due to the prolonged sampling period of 2 minutes in PET images. In study II, the PET segmentations in 4D-PET and 3D-PET influenced by respiratory motions were evaluated according to static PET acquisition in terms of volume change and the amount of low-uptake activity segmentations. Due to the study design based on phantom measurements, this association to the static PET acquisitions diverge from the basic assumption (ground truth), that quantifies segmentations according to the surgical specimens (60;61;86). The preferred segmentation methods in study II have previous been correlated to the actual lesion sizes in phantom studies and to surgical specimens from clinical trials. Segmentation misinterpretations in the static PET image were not addressed and the associations with static PET images in study II required reliable segmentation within stationary images according to ground truth. Hence, the different activity levels in the high- and lowUptake sub-volumes could lead to different SUV threshold levels for accurate segmentations. The limited target constellations, tracer activity levels and ratios between high- and lowUptake volumes, investigated in the study may not reveal a complete behaviour of the segmentation methods. In comparison, Berthon et al. evaluated segmentations of various target shapes for stationary PET images (87). That particular study revealed reduced DSC for toroid-shaped target segmentated by watershed transform, which is closely related to GradientSeg used in study II. The four segmentation methods presented segmentations in 4D-PET that were close to the static PET

segmentations, which is in agreement with the work by Bettinardi et al. for equivalent target sizes and amplitude of motion (55). Using 4D-PET as a gold standard for moving target lesions, the additional time needed to collect equal counts, such as in 3D-PET, must be considered in clinical practice according to tissue location and deformation. The segmentation methods GradientSeg and 2.5SUV both delivered segmentation results in the motion deblurred PET images equivalent to the segmentations in static PET images. Therefore, no additional time is needed, unlike 4D-PET acquisition. The other two segmentation methods Max40% and SUV40% in study II, presented some disagreement for deblurred motion-correction images in the similarity metrics ΔVol and lowUptake$_{error}$. In particular, the GradientSeg method largely overestimated the segmented volume as well as the lowUptake$_{error}$ quantity for non-corrected 3D-PET images. For potential absence of non-corrected 3D-PET images or images acquired without 4D-PET the GradientSeg method should be avoided due to the risk of misinterpretion of the segmented target lesion. Alternatively, combining multiple segmentation methods using majority vote or simultaneous truth and performance level estimation has been proposed (88). This study investigated the combination of segmentation methods (includning Max40% and GradientSeg used in study II) and revealed high accuracy for both DSC and average surface distances when segmentation methods were combined. This approach should be of particular interest when applying for a segmentation method prone to error in special cases such as with motion, heterogeneous tracer activity or distinct target shapes. 3D-PET image correction using 4D-CT might be possible for a clinical purpose. Motion deblurring using a position probability estimate rely on an accurate process for 4D-CT target tracking. Fiducials or unique anatomical landmarks, such as those used in study I and study III, can potentially allow for 4D-CT assessed target trajectory intended for 3D-PET motion deblurring. This allow in particular for GradientSeg method, segmentations in motion-included PET images equivalent to 4D-PET and the stationary 3D-PET image acquisitions. In study II, the position probability kernel was derived using a CT-defined target volume through the complete 4D-CT. This position density kernel can be estimated using fiducials as well. For motion deblurring with position density estimate through fiducial tracking in 4D-CT the individual fiducials must be positioned near each target lesion due to the site depended respiratory trajectories (84). Alternatively, some bronchial branch point, could be used to identify the different repiratory trajectories, if detection is possible in each CT phase. The accuracy of corresponding landmarks was compared to the Dice similarity coefficients of the overall body volumes as well as the lungs. Comparing the Dice coefficient with distinct landmarks for validation of image registration, may bias the validation in favour of deformable registration algorithms. All three algorithms performed image registrations with optimizations based on image intensity values. With the restricted degree of freedom in the Affine algorithm with the absence of local deformations, the overall patient volume would be a high priority for the

optimizer in the Affine algorithms. A large volume of interest, such as the thorax, may consequently disregard highly accurate local similarities such as the bronchial branch point. The advantage of deformable thoracic image registration has been addressed by Senti et al. with user-defined anatomical landmarks for validation (89). The study by Senti et al. revealed an improvement of 3 mm for the bronchial branches in favour of deformable registration methods, which is similar to the finding in study III. Alternative, a study by Castillo et al. manually identified numerous vessel bifurcations in the lungs as landmarks to validate thoracic CT co-registration (90). The average displacement was from 4 mm to just over 9 mm in five patient cases, with a maximum deviation from 13 to almost 25 mm. The maximum deviation correspond to the maximum deviations found in study III; however, the average deviations were higher in the study by Castillo et al. The larger number of landmarks and increased amount of thoracic volume coverage of these landmarks, most likely explains this difference. The accuracy of the corresponding bronchial branch point was significantly increased for the B-spline registration algorithm compared with the Demons algorithm. This improved accuracy of the B-spline algorithm was assessed for the bronchial branch point deviations, as no differences were found between the B-spline and Demons algorithms in terms of Dice similarities for either body or lung volumes. Similarly superior accuracy for a B-spline against a Demons registration was published by Varadhan et al. (91). Despite the overall improved accuracy with the B-spline and Demons algorithms, the validation methods revealed a potential risk of local misalignments within these algorithms. For the B-spline algorithm, a local registration error of 16 mm was detected in the upper lung, which indeed was associated with the highest accuracy. Additionally, the presence of image heterogeneity as intensity gradients influences the accuracy of the DIR algorithms (92). In healthy lung tissue, the bronchial airways provide heterogeneous CT densities in the lung region. Lack of CT intensity heterogeneity in the lung region could be due to the presence of atelectasis, bulky tumour lesions or lung density change due to pneumonitis or fibrosis (93-95). None of the five patients in study III were diagnosed with bulk tumours near the lung volumes, and none of the patients received thoracic radiotherapy within the periods of CT acquisitions. The anatomical changes related to bulky tumours and radiotherapy in the volume of interest for image registration may influence the accuracy of thoracic image registration. The influence of these CT density variations was not addressed in study III and need further research for clinical application. With the automatical extraction followed by unique labelling of bronchial branch points used in study III the anatomical landmarks can potentially serve as features for image registration. This was demonstrated by Vasquez Osorios et al. for multimodal image registration (CT-MRI) of the liver using vessel segmentation as landmark features (96). The combinations of features such as bronchial branch points and intensity-based image

registrations may potentially prevent the unrealistic registration as observed in the B-spline and Demons registration methods.

CHAPTER 8. FUTURE PERSPECTIVES

Assesment of uncertainties in radiotherapy is an on-going process, where previous findings are updated each time conditions have changed. This could for instance be a new imaging technique, fiducial type, target segmentation method or image registration procedure.

Fiducials in the bronchial airway tree are appropriate for both feature based image registration and validation of image registration between image modalities as CT and MRI. If the fiducials are excluded in the image registration optimization process, they could be used as an independed validation tool. Thus, intensity or feature based image registration could be assisted by a grid of anatomical landmarks like the bronchial branch points and validated using fiducials. Alternatively, the corresponding bronchial branch points could be implemented with an intensity-based image registration method, as a restriction metric to avoid unrealistic deformations. Another perspective with anatomical features as bronchial branch point is the possibility to perform a full automatic feature based image registration, using the corresponding bronchial branch points alone. This kind of automatic image registration is likely to involve a unique atlas based identification and labelling of the bronchial branch points.

Assessment of FDG-PET segmentation uncertainties, does not only apply for lung cancer, as degraded PET images caused by motions concern other cancer locations as well. Furthermore, the uncertainties in the FDG-PET target definition and image registration does not only apply for radiotherapy. Accurate target definition and OAR identification are highly relevant for the planning stage in relation to surgery or radiofrequency ablation. As these treatments are limited to restricted tumour positions, an accurate target segmentation is necessary, as provided by the GradientSeg method in 4D-PET and motion corrected 3D-PET images. Combined with accurate bronchial airway segmentation and identification of incorrect image registration, the outcomes in this thesis might find perspective outside the field of radiotherapy.

CHAPTER 9. CONCLUSIONS

Based on the three papers the most important conclusions of this PhD thesis are as follows:

The uncertainties of fiducials as surrogates in 4D-CT correlate to speed during phase bin acquisition.

Using a 5mm NiTi stent requires additional margins for radiotherapy planning in the mid-ventilation CT phase of a 4D-CT.

No 4D-CT fiducial detection differences were found between CT slice thicknesses of 1.25 & 2.50 mm for the investigated fiducials.

FDG-PET phantom lesions with heterogeneous tracer distribution revealed discrepancies between commonly used segmentation methods for motion-involved image acquisitions.

PET segmentations in 4D-PET images and motion corrected 3D-PET images were most consistent with stationary PET images segmentation using the GradientSeg method.

The 2.5SUV segmentation method was for 3D-PET images acquired with residual motion most consistent to segmentation in stationary image.

Validation of thoracic CT-CT image registration using the bronchial branch points, revealed discrepancies between the investigated registration methods, comparable to discrepancies found with volumetric Dice similarities.

Of the investigated registration methods, the B-spline registration algorithm presented the lowest overall deviations between corresponding bronchial branch points.

Position of local registration errors can be detected using extracted bronchial branch points as a validation tool in image registration.

Literature list

(1) Engholm G, Ferlay J, Christensen N, Bray F, Gjerstorff ML, Klint A, et al. NORDCAN: Cancer Incidence, Martality, Prevalence and Survival in the Nordic Contries, Version 7.1 (09.07.2015). Association of the Nordic Cancer Registries. Danish Cancer Society. Available from http://www.ancr.nu.

(2) Editor: Rasmussen TR. Dansk Lunge Cancer Register årsrapport 2013, Nov 11th.

(3) de GP, Munden RF. Lung cancer epidemiology, risk factors, and prevention. Radiol Clin North Am 2012 Sep;50(5):863-76.

(4) Boyle P. Cancer, cigarette smoking and premature death in Europe: a review including the Recommendations of European Cancer Experts Consensus Meeting, Helsinki, October 1996. Lung Cancer 1997 May;17(1):1-60.

(5) Shopland DR. Tobacco use and its contribution to early cancer mortality with a special emphasis on cigarette smoking. Environ Health Perspect 1995 Nov;103 Suppl 8:131-42.

(6) Goldstraw P, Editor. Staging Manual in Thoracic Oncology. International Association For The Study of Lung Cancer. 2009 Jul 1.

(7) Editor: Hansen O. DOLG's Radioterapigruppens Rekommendationer for udførelse af strålebehandling ved lungekræft. Available from: http://www.dolg.dk.

(8) Corso CD, Rutter CE, Park HS, Lester-Coll NH, Kim AW, Wilson LD, et al. Role of Chemoradiotherapy in Elderly Patients With Limited-Stage Small-Cell Lung Cancer. J Clin Oncol 2015 Dec 20;33(36):4240-6.

(9) O'Rourke N, Roque IF, Farre BN, Macbeth F. Concurrent chemoradiotherapy in non-small cell lung cancer. Cochrane Database Syst Rev 2010;(6):CD002140.

(10) Flores RM, Alam N. Video-assisted thoracic surgery lobectomy (VATS), open thoracotomy, and the robot for lung cancer. Ann Thorac Surg 2008 Feb;85(2):S710-S715.

(11) Whitson BA, Groth SS, Duval SJ, Swanson SJ, Maddaus MA. Surgery for early-stage non-small cell lung cancer: a systematic review of the video-assisted thoracoscopic surgery versus thoracotomy approaches to lobectomy. Ann Thorac Surg 2008 Dec;86(6):2008-16.

(12) Chang JY, Senan S, Paul MA, Mehran RJ, Louie AV, Balter P, et al. Stereotactic ablative radiotherapy versus lobectomy for operable stage I non-small-cell lung cancer: a pooled analysis of two randomised trials. Lancet Oncol 2015 Jun;16(6):630-7.

(13) Jeppesen SS, Schytte T, Jensen HR, Brink C, Hansen O. Stereotactic body radiation therapy versus conventional radiation therapy in patients with early stage non-small cell lung cancer: an updated retrospective study on local failure and survival rates. Acta Oncol 2013 Oct;52(7):1552-8.

(14) Lindberg K, Nyman J, Riesenfeld K, V, Hoyer M, Lund JA, Lax I, et al. Long-term results of a prospective phase II trial of medically inoperable stage I NSCLC treated with S. Acta Oncol 2015;54(8):1096-104.

(15) Zhang XJ, Sun JG, Sun J, Ming H, Wang XX, Wu L, et al. Prediction of radiation pneumonitis in lung cancer patients: a systematic review. J Cancer Res Clin Oncol 2012 Dec;138(12):2103-16.

(16) Allibhai Z, Taremi M, Bezjak A, Brade A, Hope AJ, Sun A, et al. The impact of tumor size on outcomes after stereotactic body radiation therapy for medically inoperable early-stage non-small cell lung cancer. Int J Radiat Oncol Biol Phys 2013 Dec 1;87(5):1064-70.

(17) Akhan O, Guler E, Akinci D, Ciftci T, Kose IC. Radiofrequency ablation for lung tumors: outcomes, effects on survival, and prognostic factors. Diagn Interv Radiol 2016 Jan;22(1):65-71.

(18) Bilal H, Mahmood S, Rajashanker B, Shah R. Is radiofrequency ablation more effective than stereotactic ablative radiotherapy in patients with early stage medically inoperable non-small cell lung cancer? Interact Cardiovasc Thorac Surg 2012 Aug;15(2):258-65.

(19) Simon CJ, Dupuy DE, Dipetrillo TA, Safran HP, Grieco CA, Ng T, et al. Pulmonary radiofrequency ablation: long-term safety and efficacy in 153 patients. Radiology 2007 Apr;243(1):268-75.

(20) Marks LB, Bentzen SM, Deasy JO, Kong FM, Bradley JD, Vogelius IS, et al. Radiation dose-volume effects in the lung. Int J Radiat Oncol Biol Phys 2010 Mar 1;76(3 Suppl):S70-S76.

(21) Vogelius IR, Bentzen SM. A literature-based meta-analysis of clinical risk factors for development of radiation induced pneumonitis. Acta Oncol 2012 Nov;51(8):975-83.

(22) Aristophanous M, Berbeco RI, Killoran JH, Yap JT, Sher DJ, Allen AM, et al. Clinical utility of 4D FDG-PET/CT scans in radiation treatment planning. Int J Radiat Oncol Biol Phys 2012 Jan 1;82(1):e99-105.

(23) Mac Manus MP, Hicks RJ. The role of positron emission tomography/computed tomography in radiation therapy planning for patients with lung cancer. Semin Nucl Med 2012 Sep;42(5):308-19.

(24) Abdelnour AF, Nehmeh SA, Pan T, Humm JL, Vernon P, Schoder H, et al. Phase and amplitude binning for 4D-CT imaging. Phys Med Biol 2007 Jun 21;52(12):3515-29.

(25) Keall PJ, Mageras GS, Balter JM, Emery RS, Forster KM, Jiang SB, et al. The management of respiratory motion in radiation oncology report of AAPM Task Group 76. Med Phys 2006 Oct;33(10):3874-900.

(26) International Commission on Radioation Units and Measurements. ICRU Report 62. Prescribing, recording and reporting photon beam therapy (Supplement to ICRU Report 50). Bethesda, MD: ICRU, 1999. 2015.

(27) van HM, Remeijer P, Rasch C, Lebesque JV. The probability of correct target dosage: dose-population histograms for deriving treatment margins in radiotherapy. Int J Radiat Oncol Biol Phys 2000 Jul 1;47(4):1121-35.

(28) International Commission on Radioation Units and Measurements. ICRU Report 50. Prescribing, recording and reporting photon beam therapy. Bethesda, MD: ICRU, 1993. 2015.

(29) De RD, Faivre-Finn C, Nestle U, Hurkmans CW, Le PC, Price A, et al. European Organisation for Research and Treatment of Cancer recommendations for planning and delivery of high-dose, high-precision radiotherapy for lung cancer. J Clin Oncol 2010 Dec 20;28(36):5301-10.

(30) Gagliardi G, Constine LS, Moiseenko V, Correa C, Pierce LJ, Allen AM, et al. Radiation dose-volume effects in the heart. Int J Radiat Oncol Biol Phys 2010 Mar 1;76(3 Suppl):S77-S85.

(31) Werner-Wasik M, Yorke E, Deasy J, Nam J, Marks LB. Radiation dose-volume effects in the esophagus. Int J Radiat Oncol Biol Phys 2010 Mar 1;76(3 Suppl):S86-S93.

(32) Jaffray DA, Lindsay PE, Brock KK, Deasy JO, Tome WA. Accurate accumulation of dose for improved understanding of radiation effects in normal tissue. Int J Radiat Oncol Biol Phys 2010 Mar 1;76(3 Suppl):S135-S139.

(33) Kong FM, Pan C, Eisbruch A, Ten Haken RK. Physical models and simpler dosimetric descriptors of radiation late toxicity. Semin Radiat Oncol 2007 Apr;17(2):108-20.

(34) Lyman JT. Complication probability as assessed from dose-volume histograms. Radiat Res Suppl 1985;8:S13-S19.

(35) Emami B, Lyman J, Brown A, Coia L, Goitein M, Munzenrider JE, et al. Tolerance of normal tissue to therapeutic irradiation. Int J Radiat Oncol Biol Phys 1991 May 15;21(1):109-22.

(36) Gay HA, Niemierko A. A free program for calculating EUD-based NTCP and TCP in external beam radiotherapy. Phys Med 2007 Dec;23(3-4):115-25.

(37) Barriger RB, Forquer JA, Brabham JG, Andolino DL, Shapiro RH, Henderson MA, et al. A dose-volume analysis of radiation pneumonitis in non-small cell lung cancer patients treated with stereotactic body radiation therapy. Int J Radiat Oncol Biol Phys 2012 Jan 1;82(1):457-62.

(38) Matsuo Y, Shibuya K, Nakamura M, Narabayashi M, Sakanaka K, Ueki N, et al. Dose--volume metrics associated with radiation pneumonitis after stereotactic body radiation therapy for lung cancer. Int J Radiat Oncol Biol Phys 2012 Jul 15;83(4):e545-e549.

(39) Seppenwoolde Y, Lebesque JV, De JK, Belderbos JS, Boersma LJ, Schilstra C, et al. Comparing different NTCP models that predict the incidence of radiation pneumonitis. Normal tissue complication probability. Int J Radiat Oncol Biol Phys 2003 Mar 1;55(3):724-35.

(40) De WW, Ceyssens S, Mortelmans L, Stroobants S, Marchal G, Bogaert J, et al. Additional value of PET-CT in the staging of lung cancer: comparison with CT alone, PET alone and visual correlation of PET and CT. Eur Radiol 2007 Jan;17(1):23-32.

(41) Shim SS, Lee KS, Kim BT, Chung MJ, Lee EJ, Han J, et al. Non-small cell lung cancer: prospective comparison of integrated FDG PET/CT and CT alone for preoperative staging. Radiology 2005 Sep;236(3):1011-9.

(42) Steenbakkers RJ, Duppen JC, Fitton I, Deurloo KE, Zijp LJ, Comans EF, et al. Reduction of observer variation using matched CT-PET for lung cancer delineation: a three-dimensional analysis. Int J Radiat Oncol Biol Phys 2006 Feb 1;64(2):435-48.

(43) Konert T, Vogel W, MacManus MP, Nestle U, Belderbos J, Gregoire V, et al. PET/CT imaging for target volume delineation in curative intent radiotherapy of non-small cell lung cancer: IAEA consensus report 2014. Radiother Oncol 2015 Jul;116(1):27-34.

(44) Keall PJ, Vedam SS, George R, Williamson JF. Respiratory regularity gated 4D CT acquisition: concepts and proof of principle. Australas Phys Eng Sci Med 2007 Sep;30(3):211-20.

(45) Rietzel E, Pan T, Chen GT. Four-dimensional computed tomography: image formation and clinical protocol. Med Phys 2005 Apr;32(4):874-89.

(46) Wolthaus JW, Schneider C, Sonke JJ, van HM, Belderbos JS, Rossi MM, et al. Mid-ventilation CT scan construction from four-dimensional respiration-correlated CT scans for radiotherapy planning of lung cancer patients. Int J Radiat Oncol Biol Phys 2006 Aug 1;65(5):1560-71.

(47) Nakamura M, Narita Y, Sawada A, Matsugi K, Nakata M, Matsuo Y, et al. Impact of motion velocity on four-dimensional target volumes: a phantom study. Med Phys 2009 May;36(5):1610-7.

(48) Pan T, Lee TY, Rietzel E, Chen GT. 4D-CT imaging of a volume influenced by respiratory motion on multi-slice CT. Med Phys 2004 Feb;31(2):333-40.

(49) Persson GF, Nygaard DE, Af Rosenschold PM, Richter V, I, Josipovic M, Specht L, et al. Artifacts in conventional computed tomography (CT) and free breathing four-dimensional CT induce uncertainty in gross tumor volume determination. Int J Radiat Oncol Biol Phys 2011 Aug 1;80(5):1573-80.

(50) Lu W, Parikh PJ, Hubenschmidt JP, Bradley JD, Low DA. A comparison between amplitude sorting and phase-angle sorting using external respiratory measurement for 4D CT. Med Phys 2006 Aug;33(8):2964-74.

(51) De RD, Nestle U, Jeraj R, MacManus M. PET scans in radiotherapy planning of lung cancer. Lung Cancer 2012 Feb;75(2):141-5.

(52) Tong S, Alessio AM, Kinahan PE. Image reconstruction for PET/CT scanners: past achievements and future challenges. Imaging Med 2010 Oct 1;2(5):529-45.

(53) Callahan J, Binns D, Dunn L, Kron T. Motion effects on SUV and lesion volume in 3D and 4D PET scanning. Australas Phys Eng Sci Med 2011 Dec;34(4):489-95.

(54) Hatt M, Cheze-Le RC, van BA, Lambin P, Pradier O, Visvikis D. Impact of tumor size and tracer uptake heterogeneity in (18)F-FDG PET and CT non-small cell lung cancer tumor delineation. J Nucl Med 2011 Nov;52(11):1690-7.

(55) Bettinardi V, Rapisarda E, Gilardi MC. Number of partitions (gates) needed to obtain motion-free images in a respiratory gated 4D-PET/CT study as a function of the lesion size and motion displacement. Med Phys 2009 Dec;36(12):5547-58.

(56) El N, I, Low DA, Bradley JD, Vicic M, Deasy JO. Deblurring of breathing motion artifacts in thoracic PET images by deconvolution methods. Med Phys 2006 Oct;33(10):3587-600.

(57) Reyes M, Malandain G, Koulibaly PM, Gonzalez-Ballester MA, Darcourt J. Model-based respiratory motion compensation for emission tomography image reconstruction. Phys Med Biol 2007 Jun 21;52(12):3579-600.

(58) Thie JA. Understanding SUV variability in reference tissue for 18F-FDG PET with a simple measurement model. J Nucl Med 2014 Feb;55(2):352.

(59) Biehl KJ, Kong FM, Dehdashti F, Jin JY, Mutic S, El N, I, et al. 18F-FDG PET definition of gross tumor volume for radiotherapy of non-small cell lung cancer: is a single standardized uptake value threshold approach appropriate? J Nucl Med 2006 Nov;47(11):1808-12.

(60) Werner-Wasik M, Nelson AD, Choi W, Arai Y, Faulhaber PF, Kang P, et al. What is the best way to contour lung tumors on PET scans? Multiobserver validation of a gradient-based method using a NSCLC digital PET phantom. Int J Radiat Oncol Biol Phys 2012 Mar 1;82(3):1164-71.

(61) Yu J, Li X, Xing L, Mu D, Fu Z, Sun X, et al. Comparison of tumor volumes as determined by pathologic examination and FDG-PET/CT

images of non-small-cell lung cancer: a pilot study. Int J Radiat Oncol Biol Phys 2009 Dec 1;75(5):1468-74.

(62) Aristophanous M, Penney BC, Martel MK, Pelizzari CA. A Gaussian mixture model for definition of lung tumor volumes in positron emission tomography. Med Phys 2007 Nov;34(11):4223-35.

(63) Geets X, Lee JA, Bol A, Lonneux M, Gregoire V. A gradient-based method for segmenting FDG-PET images: methodology and validation. Eur J Nucl Med Mol Imaging 2007 Sep;34(9):1427-38.

(64) Wanet M, Lee JA, Weynand B, De BM, Poncelet A, Lacroix V, et al. Gradient-based delineation of the primary GTV on FDG-PET in non-small cell lung cancer: a comparison with threshold-based approaches, CT and surgical specimens. Radiother Oncol 2011 Jan;98(1):117-25.

(65) Korreman S, Persson G, Nygaard D, Brink C, Juhler-Nottrup T. Respiration-correlated image guidance is the most important radiotherapy motion management strategy for most lung cancer patients. Int J Radiat Oncol Biol Phys 2012 Jul 15;83(4):1338-43.

(66) Kupelian PA, Forbes A, Willoughby TR, Wallace K, Manon RR, Meeks SL, et al. Implantation and stability of metallic fiducials within pulmonary lesions. Int J Radiat Oncol Biol Phys 2007 Nov 1;69(3):777-85.

(67) Murphy MJ. Fiducial-based targeting accuracy for external-beam radiotherapy. Med Phys 2002 Mar;29(3):334-44.

(68) Bhagat N, Fidelman N, Durack JC, Collins J, Gordon RL, LaBerge JM, et al. Complications associated with the percutaneous insertion of fiducial markers in the thorax. Cardiovasc Intervent Radiol 2010 Dec;33(6):1186-91.

(69) Yousefi S, Collins BT, Reichner CA, Anderson ED, Jamis-Dow C, Gagnon G, et al. Complications of thoracic computed tomography-guided fiducial placement for the purpose of stereotactic body radiation therapy. Clin Lung Cancer 2007 Jan;8(4):252-6.

(70) Carl J, Jensen HK, Nielsen J, Nielsen MS, Schmid M, Siegfried L. A New Fiducial Marker for Gated Radiotherapy in the Lung – A Feasibility Study of Bronchoscopy Based Insertion and Removal in Göttingen Mini-Pig. Scandinavian Journal of Laboratory Animal Science 2010;37(2):117-27.

(71) Carl J, Nielsen J, Nielsen MS, Zepernick PR, Kjaergaard B, Jensen HK. A new lung stent tested as fiducial marker in a porcine model. Radiother Oncol 2012 Feb;102(2):297-302.

(72) Poulsen PR, Carl J, Nielsen J, Nielsen MS, Thomsen JB, Jensen HK, et al. Megavoltage image-based dynamic multileaf collimator tracking of a NiTi stent in porcine lungs on a linear accelerator. Int J Radiat Oncol Biol Phys 2012 Feb 1;82(2):e321-e327.

(73) Oliveira FP, Tavares JM. Medical image registration: a review. Comput Methods Biomech Biomed Engin 2014;17(2):73-93.

(74) Sotiras A, Davatzikos C, Paragios N. Deformable medical image registration: a survey. IEEE Trans Med Imaging 2013 Jul;32(7):1153-90.

(75) Holden M. A review of geometric transformations for nonrigid body registration. IEEE Trans Med Imaging 2008 Jan;27(1):111-28.

(76) Thirion JP. Image matching as a diffusion process: an analogy with Maxwell's demons. Med Image Anal 1998 Sep;2(3):243-60.

(77) Zhao YR, van Ooijen PM, Dorrius MD, Heuvelmans M, de Bock GH, Vliegenthart R, et al. Comparison of three software systems for semi-automatic volumetry of pulmonary nodules on baseline and follow-up CT examinations. Acta Radiol 2014 Jul;55(6):691-8.

(78) Kadoya N, Fujita Y, Katsuta Y, Dobashi S, Takeda K, Kishi K, et al. Evaluation of various deformable image registration algorithms for thoracic images. J Radiat Res 2014 Jan 1;55(1):175-82.

(79) Murphy K, van Ginneken B, Reinhardt JM, Kabus S, Ding K, Deng X, et al. Evaluation of registration methods on thoracic CT: the EMPIRE10 challenge. IEEE Trans Med Imaging 2011 Nov;30(11):1901-20.

(80) Petrou M, Quint LE, Nan B, Baker LH. Pulmonary nodule volumetric measurement variability as a function of CT slice thickness and nodule morphology. AJR Am J Roentgenol 2007 Feb;188(2):306-12.

(81) Sinsuat M, Saita S, Kawata Y, Niki N, Ohmatsu H, Tsuchida T, et al. Influence of slice thickness on diagnoses of pulmonary nodules using low-dose CT: potential dependence of detection and diagnostic agreement on features and location of nodule. Acad Radiol 2011 May;18(5):594-604.

(82) Matney JE, Parker BC, Neck DW, Henkelmann G, Rosen II. Target localization accuracy in a respiratory phantom using BrainLAB ExacTrac and 4DCT imaging. J Appl Clin Med Phys 2011;12(2):3296.

(83) Wolthaus JW, Sonke JJ, van HM, Belderbos JS, Rossi MM, Lebesque JV, et al. Comparison of different strategies to use four-dimensional computed tomography in treatment planning for lung cancer patients. Int J Radiat Oncol Biol Phys 2008 Mar 15;70(4):1229-38.

(84) Seppenwoolde Y, Shirato H, Kitamura K, Shimizu S, van HM, Lebesque JV, et al. Precise and real-time measurement of 3D tumor motion in lung due to breathing and heartbeat, measured during radiotherapy. Int J Radiat Oncol Biol Phys 2002 Jul 15;53(4):822-34.

(85) Korreman SS, Juhler-Nottrup T, Boyer AL. Respiratory gated beam delivery cannot facilitate margin reduction, unless combined with respiratory correlated image guidance. Radiother Oncol 2008 Jan;86(1):61-8.

(86) Foster B, Bagci U, Mansoor A, Xu Z, Mollura DJ. A review on segmentation of positron emission tomography images. Comput Biol Med 2014 Jul;50:76-96.

(87) Berthon B, Marshall C, Evans M, Spezi E. Evaluation of advanced automatic PET segmentation methods using nonspherical thin-wall inserts. Med Phys 2014 Feb;41(2):022502.

(88) McGurk RJ, Bowsher J, Lee JA, Das SK. Combining multiple FDG-PET radiotherapy target segmentation methods to reduce the effect of variable performance of individual segmentation methods. Med Phys 2013 Apr;40(4):042501.

(89) Senthi S, Griffioen GH, van Sornsen de Koste JR, Slotman BJ, Senan S. Comparing rigid and deformable dose registration for high dose thoracic re-irradiation. Radiother Oncol 2013 Mar;106(3):323-6.

(90) Castillo R, Castillo E, Guerra R, Johnson VE, McPhail T, Garg AK, et al. A framework for evaluation of deformable image registration spatial accuracy using large landmark point sets. Phys Med Biol 2009 Apr 7;54(7):1849-70.

(91) Varadhan R, Karangelis G, Krishnan K, Hui S. A framework for deformable image registration validation in radiotherapy clinical applications. J Appl Clin Med Phys 2013;14(1):4066.

(92)   Zhong H, Kim J, Chetty IJ. Analysis of deformable image registration accuracy using computational modeling. Med Phys 2010 Mar;37(3):970-9.

(93)   Chow TL, Louie AV, Palma DA, D'Souza DP, Perera F, Rodrigues GB, et al. Radiation-induced lung injury after concurrent neoadjuvant chemoradiotherapy for locally advanced breast cancer. Acta Oncol 2014 May;53(5):697-701.

(94)   De Ruysscher D, Sharifi H, Defraene G, Kerns SL, Christiaens M, De Ruyck K, et al. Quantification of radiation-induced lung damage with CT scans: the possible benefit for radiogenomics. Acta Oncol 2013 Oct;52(7):1405-10.

(95)   Sorensen L, Loog M, Lo P, Ashraf H, Dirksen A, Duin RP, et al. Image dissimilarity-based quantification of lung disease from CT. Med Image Comput Comput Assist Interv 2010;13(Pt 1):37-44.

(96)   Vasquez Osorio EM, Hoogeman MS, Mendez RA, Wielopolski P, Zolnay A, Heijmen BJ. Accurate CTMR vessel-guided nonrigid registration of largely deformed livers. Med Phys 2012 May;39(5):2463-77.